Università degli Studi di Padova
Dipartimento di Fisica ed Astronomia “G. Galilei”

Laurea Magistrale in Fisica

Lasing action in dye-doped thin films coupled with 2D plasmonic nanoarrays

Laureando:
Diego Piccotti

Relatrice:
Dott.ssa Tiziana Cesca

Controrelatore:
Dott. Marco Bazzan

Correlatore:
Prof. Giovanni Mattei

Anno Accademico 2015/2016

To Martina, my family
and my friends.

"There's Plenty of Room at the Bottom"
Richard Feynman (1959)

Abstract

In the last few years due to the great advances in nanotechnology, the peculiar properties of the matter at the nanometric scale have been widely investigated. These properties can be exploited for many innovative applications involving several fields, and, in particular, in nanophotonics, where plasmonic nanolasers gather growing interest.
These devices are coherent light sources that can support ultrafast dynamics and ultra-small mode volume below the $\lambda/2$ diffraction limit. Nowadays, the photonic band-edge lasers that are widely used for many applications have various drawbacks, such as low modulation speeds and diffraction-limited mode confinement.
Plasmonic nanolasers can potentially overcome these limits and replace the actual light source technology in many fields from integrated photonic circuits and optical communications to high-performance biosensors.

The purpose of the present Master thesis is the synthesis and characterisation of a novel plasmonic-based nanolaser device operating in the near infrared-region. In particular, the attention has been focused on plasmonic nanostructures composed of an 2D array of nanoparticles that acts as field enhancer for the lasing of the gain medium. The fabrication of the plasmonic nanoarray was substantially different from the usual approach based on electron beam lithography (EBL). On the contrary, the NanoSphere Lithography (NSL) technique adopted in the present thesis is a high-throughput and cost-effective way to manufacture nanoparticle arrays with a high-quality order, obtaining defectless domains of several hundreds of μm^2.

The nanostructure adopted in a this work is two-dimensional hexagonal lattice of nanodomes which is fabricated by gold deposition (carried out by magnetron sputtering) over an ordered array of polystyrene (PS) nanospheres (NSs) obtained using NSL. A gain medium layer was then deposited over the metallic array, and it consists of an organic dye, specifically *Styryl 9M* (LDS 821), embedded in a polymeric matrix.
In order to maximise the efficiency and the throughput of the nanolaser, a match between the fluorescence emission of the selected dye and the plasmonic resonance of the nanostructure is needed. To this aim, the domes geometry has been optimised by varying metal thickness and the PS nanosphere radius (while keeping the array lattice parameter) by reactive ion etching (RIE).
The deposition process for the gain medium has been achieved by embedding the dye molecules in a PMMA matrix, which is then deposited upon the nanodome array to form a solid film of a hundred of micrometers. The nanostructures have been characterised morphologically by atomic force microscopy (AFM) and scanning electron microscopy (SEM) techniques and optically by reflection measurements. The absorption

and fluorescence spectra that characterise the dye were measured by a UV-VIS-NIR spectrophotometry.

As a result, samples supporting lasing action were fabricated and characterised: the emission features of the obtained device were investigated by photoluminescence (PL) measurements to determine the main properties of the laser, including the lasing wavelength, linewidth, threshold, beam divergence and emission angle, showing how, when a coupling between the plasmonic resonance of the nanodome array and the dye emission wavelength is obtained, interesting lasing properties arise and the lasing threshold can be decreased by at least one order of magnitude.

Estratto

Negli ultimi anni, affascinanti proprietà della materia su scala nanometrica sono state ampiamente studiate grazie ai grandi progressi nelle nanotecnologie. Queste proprietà possono essere sfruttate per molte applicazioni innovative che coinvolgono diversi campi, e, in particolare, in nanofotonica, dove i nanolaser plasmonici riscuotono crescente interesse.
Questi dispositivi sono sorgenti di luce coerente in grado di supportare dinamiche ultraveloci e modi di volume ultrapiccoli al di sotto del limite di diffrazione $\lambda/2$. Al giorno d'oggi, i laser a bordo-banda che sono ampiamente usati in molte applicazioni presentano diversi inconvenienti, come ad esempio basse velocità di modulazione e modi di volume limitati dal limite di diffrazione.
I nanolaser plasmonici possono potenzialmente superare questi limiti e sostituire l'attuale tecnologia di sorgente luminosa in molti campi, da circuiti fotonici integrati a comunicazioni ottiche, fino a biosensori ad alte prestazioni.

Lo scopo della presente tesi magistrale è la sintesi e la caratterizzazione di un nuovo dispositivo nanolaser basato su proprietà plasmoniche. In particolare, l'attenzione è stata focalizzata su nanostrutture plasmoniche composte da un reticolo bidimensionale di nanoparticelle che agisce come amplicatore di campo per l'azione laser del mezzo attivo. La fabbricazione del reticolo plasmonico è sostanzialmente diversa dal più usato approccio di litografia a fascio elettronico (EBL). Al contrario, la tecnica denominata litografia a nanosfere (NSL), adottata nel presente lavoro, è un modo più economico per la produzione di estese matrici di nanoparticelle con un'alta qualità sull'ordine, ottenendo domini privi di difetti di diverse centinaia di μm^2 .

La nanostruttura adottata in questo lavoro è un reticolo bidimensionale esagonale di nanocupole, che è stato fabbricato eseguendo una deposizione di oro (svolta attraverso *"magnetron sputtering"*) su una serie ordinata di nanosfere di polistirene ottenuta mediante NSL. Quindi è stato depositato sulla matrice metallica un film di materiale attivo, costituito da molecole organiche di colorante, nello specifico *Styryl 9M* (LDS 821), immerse in una matrice polimerica. Per massimizzare l'efficienza del nanolaser, è necessaria una sovrapposizione tra l'emissione in fluorescenza della molecola colorante e la risonanza plasmonica della nanostruttura. A questo scopo, le caratteristiche della cupola sono state ottimizzate variando lo spessore del metallo e il raggio delle nanosfere di polistirene (mantenendo la costante reticolare) mediante *Reactive Ion Etching* (RIE).
Il processo di deposizione per il mezzo di guadagno è stato ottenuto drogando una matrice di PMMA con molecole di colorante. Il film viene quindi depositato sul reticolo di nanocupole per formare un film solido di un centinaio di micrometri.

Le nanostrutture sono state caratterizzate morfologicamente al microscopio a forza atomica (AFM) e con tecniche di microscopia elettronica a scansione (SEM), oltre ad essere studiate otticamente attraverso misure in riflessione. Gli spettri di assorbimento e fluorescenza che caratterizzano il colorante sono stati misurati mediante spettrofotometria UV-VIS-NIR.

Come risultato, i campioni fabbricati che sostegno l'azione laser sono stati caratterizzati attraverso misure di fotoluminescenza (PL) per determinare le proprietà principali del laser, tra cui la lunghezza d'onda laser, la larghezza di riga, la soglia, la divergenza del fascio e l'emissione angolare, mostrando che quando si ottiene un accoppiamento tra la risonanza plasmonica della matrice di nanocupole e la lunghezza d'onda di emissione del colorante, delle interessanti proprietà di emissione di laser sorgono e la rispettiva soglia può essere ridotta notevolmente.

Contents

Introduction

Nanotechnology is the study and the manipulation of matter at the nanometric scale, where the characteristic sizes of elements put into play are comprised between one and hundreds of nanometers.

The first unaware approach of humankind with nanoparticles was discovered in the Lycurgus Cup [1] which is a IV century Roman glass chalice that show two different colors when it is illuminated in transmission or in reflection, due to the presence of gold-silver alloy nanoclusters.

In Medieval and Renaissance periods, master Giorgio Andreoli (Intra, 1465/1470 - Gubbio, 1555) used unawarely silver and copper nanoclusters to create beautiful decorations in luster pottery that shows brilliant reflections of different colours, cangiant effects and iridescence [2]. This recipe is described in the second book of "I Tre libri dell'arte del vasaio" (1557).

The first suggestion about the importance of the nanometric matter is associated to the famous talk "There is plenty of room at the bottom" held by Richard Feynman at Caltech in 1959 [3]. Feynman analysed the possibility to build machines as small as possible, up to the nanometric scale, where much care should be taken into account due to forces change: the gravitational one becomes negligible, while surface tensions and Van der Waals forces become predominant.

In 1974, Taniguchi expressed the concept of *Nanotechnology* [4] as the possibility to modify materials at the level of a single atom or molecule.

In the last thirty years, new technologies and innovative nanostructure formation methods have increased the research in the nanotechnological field. New and fascinating properties are continuously discovered and this promotes an increasing interest not only in the comprehension of matter properties at the nanoscale but also in a lot of applied fields, due to the countless potential applications that nanostructured materials can offer.

One of the most attractive area of interest in nanoscience is *Nanophtonics* which studies the behaviour of radiation at the nanoscale and the interaction between nanometric objects and light. In this field the study of the properties of electromagnetic waves-interacting metal nanostructures, in particular noble metals, is called *Plasmonics*. It proposes a control of the light confinement below the diffraction limit (namely half of the wavelength) and of the consequent enhancement of the optical near-field [5].

Among many interesting applications that plasmonics can offer, one in particular attracted me, that is the possibility to achieve laser light from the coupling between gain medium (an active material that behaves as an optical amplifier under specific conditions) and metallic ordered nanostructures. Metallic nanoparticles present resonance peaks in their optical cross-section, associated to the phenomena of *Localized Surface Plasmon Resonance* or *Surface Lattice Resonance* if we have an ordered structure. These phenomena are due to the driven harmonic motion of surface electrons of the metallic nanoparticles due to the interaction with electromagnetic wave and they have the effect of enhancing the electromagnetic field close to the particles. By spatially and spectrally matching these resonance modes with the fluorescence emission of the gain medium, nanoparticles behave as a cavity and lasing action can occur.

In general, LASER (*light amplification by stimulated emission of radiation* [6]) is a light source which is distinguished from the others by spatial and temporal coherence of emitted light, high monochromaticity and the ability to reach extremely high powers. Lasers are used in a conspicuous number of applications extending from medicine to telecommunications. Now we find them in everyday life: for example in CD/DVD/Bluray players, printers and supermarket scanners.

Material developments have given a significant contribution in laser advancement, such as the introduction of organic semiconductors that combine novel properties to simple manufacture with the possibility to tune the chemical structure to obtain desired features [7]. The recent rapid development of organic semiconductor lasers, based on light-emitting diodes which are easily found in simple displays, opens up the possibility of compact and lowcost visible lasers suitable for several applications, from diagnosis to sensing, from communications to optical circuits.

However, when we scale these devices down, they present a physical limit given by the impossibility to confine light below the diffraction limit. Luckily, as we have already said, plasmonics can give us the solution.
Regarding this topic, recent articles [8–10] have presented models and simulations of lasing action arising by coupling of a gain medium with plasmonic nanoparticle arrays, confirming not only the possibility of this phenomenon but also the reliability of these models, comparing other experimental results which came out in the meantime during these last 5 years.

The state of the art about these devices involves groups as that of T. Odom at the University of Northwestern in Illinois, or B. Cunningham at the University of Illinois, who independently use different nanostructures coupled to liquid gain media [11–14]. Also the group of A. F. Koenderink, at AMOLF in Amsterdam, is studying this kind of system, investigating the role of the nanoparticle order [15].

The purpose of my thesis is to investigate the synthesis and characterization of a novel plasmonic nanolaser device that gives rise a lasing action through dye-doped thin films coupled with a two-dimensional plasmonic nanoarray structure, synthesized by nanosphere lithography. Furthermore, the main properties of this nanolaser will be determined by studying the lasing wavelength, linewidth, threshold, beam divergence and emission angle.

The thesis will be structured as follows:

Chapter 1 will describe the theoretical treatise of the metal nanoparticle properties, after the interaction with electromagnetic waves. Then, the quasi-static approximation, we will describe the fundamental effects for a spherical nanoparticle and after that we will see the response of interacting nanoparticles in an ordered system.

Chapter 2 will illustrate the principal properties of dye molecules and their behaviour in presence of an electromagnetic field and metallic nanostructures, explaining the rise of the laser action by rate equations.

Chapter 3 will present the synthesis method with which we have fabricated our device: firstly we will analyse in detail how to create our nanoparticle arrays from nanosphere lithography to metal deposition; in addition will describe the techniques used to discriminate good lithography masks, such as optical diffraction and UV-VIS-NIR spectroscopy. Then, we will move to the process formation of the solid thin film doped with dye molecules placed upon the nanoparticles, used as gain medium.

Chapter 4 will talk about the techniques used for the characterisation of the different elements that compose the device: SEM (scanning electron microscopy) and AFM (atomic force microscopy) for the surface morphology; UV-VIS-NIR spectroscopy for optical properties of dyes and nanostructured patterns; ellipsometry for the band structure of the photonic crystal; photoluminescence (PL) spectroscopy the final laser emission characteristics.

Chapter 5 will discuss the obtained results, that is, lasing action and its characteristics but also the stability of the device undergone high pomp fluxes.

Chapter 6 will deal with the conclusion and possible future developments.

Chapter 1

Electromagnetic Waves and Metallic Nanostructures

The interaction between metallic nanostructures and electromagnetic (EM) waves can be described in a classical framework based on Maxwell's equations without the need to resort to quantum mechanics. This is true for metallic structures down to sizes of the order of few nanometers, when quantum confinement effects start to be important and the properties depend strongly on the size. In other words above size of few nanometers the high density of free carriers still results in electron energy levels with spacings smaller than thermal excitation energy $k_B T$ at room temperature [5, 16].

When an EM radiation interacts with a metal nanostructure whose size is much smaller than EM wavelength, a resonance phenomenon called *localized surface plasmon resonance* (LSPR) arises. This phenomenon is the basis of many possible applications in nanotechnologies, as a the one that will be presented in this work, i.e. the *plasmonic nanolaser*.

This chapter briefly deals with the theoretical basis of the LSPR, for more details please refer to the texts of solid state [17, 18], plasmonics [5] or nano-optics [19]. It will start with the interaction between the electromagnetic field and bulk metals, dwelling on the dielectric function. Next, the different types of plasmons will be described, focusing on interacting and not-interacting LSPs.

1.1 Electronic Properties of Metals

Although we do not use quantum mechanics, the model of interaction is not easy anyway. The description depends on both the frequency of EM field and the metal electronic structure.

Up to the far-infrared region of the radiation spectrum, namely in the low frequency regime, metals are highly reflective. So the electromagnetic waves do not propagate through the metal, only a negligible fraction of radiation penetrates to a depth called *skin depth*.

In the visible and infrared regions, the energy dissipation through the metal becomes considerable and the field penetration increases, so the model used in the low frequency region is not good to describe how metals work in this frequency range.

In the ultraviolet region, metals change their behaviour and they act as a dielectric allowing propagation of EM radiation.

These dispersive properties can be described via a *complex dielectric function* $\varepsilon(\omega)$, which provides the basis of most optical phenomena. To know $\varepsilon(\omega)$ there are various experimental or theoretical methods. A simple model is given by Drude which describes very well alkali metals in the visible range.

The starting point of the EM response of metals are the Maxwell's equations

$$\nabla \cdot \mathbf{D} = \rho_{ext} \tag{1.1a}$$

$$\nabla \cdot \mathbf{B} = 0 \tag{1.1b}$$

$$\nabla \times \mathbf{E} = -\frac{\partial \mathbf{B}}{\partial t} \tag{1.1c}$$

$$\nabla \times \mathbf{H} = \frac{\partial \mathbf{D}}{\partial t} + \mathbf{J_{ext}} \tag{1.1d}$$

where $\mathbf{E}$ is the electric field, $\mathbf{D}$ the electric displacement vector, $\mathbf{H}$ the magnetic field, $\mathbf{B}$ the magnetic induction and ρ_{ext} and $\mathbf{J_{ext}}$ are respectively external charge and current density.

The four fields are further linked via polarization $\mathbf{P}$ and magnetization $\mathbf{M}$ by

$$\mathbf{D} = \varepsilon_0 \mathbf{E} + \mathbf{P} \tag{1.2a}$$

$$\mathbf{H} = \frac{1}{\mu_0}\mathbf{B} - \mathbf{M} \tag{1.2b}$$

where ε_0 and μ_0 are the electric permittivity and the magnetic permeability of vacuum, respectively.

In this thesis only non-magnetic media will be treated, so $\mathbf{M}$ is neglected and only electric polarization effects will be taken into consideration.
The vector polarization $\mathbf{P}$ describes the electric dipole moment per unit volume inside the material and it is related to the electric field with a linear relationship [20]

$$\mathbf{P} = \varepsilon_0 \chi \mathbf{E} \tag{1.3}$$

where χ is the dielectric susceptibility, which is related to the *dielectric function* by $\varepsilon = 1 + \chi$.
The electric displacement vector can be write as

$$\mathbf{D}(\mathbf{r}, t) = \varepsilon_0 \int dt' d\mathbf{r}' \varepsilon(\mathbf{r} - \mathbf{r}', t - t') \mathbf{E}(\mathbf{r}', t') \tag{1.4}$$

By decomposition of the fields into individual plane-wave components of *wave vector* $\mathbf{K}$ and *angular frequency* ω, by *Fourier transform*, equations (1.4) are simplified significantly by turning the convolutions into multiplication

$$\mathbf{D}(\mathbf{K}, \omega) = \varepsilon_0 \, \varepsilon(\mathbf{K}, \omega) \, \mathbf{E}(\mathbf{K}, \omega) \tag{1.5}$$

The general form of the dielectric response $\varepsilon(\mathbf{K}, \omega)$ can be simplified to the limit of *spatially local* response as, $\varepsilon(\mathbf{K} = \mathbf{0}, \omega) = \varepsilon(\omega)$. This approximation is valid as long as the wavelength λ in the material is significantly longer than all the characteristic dimensions, such as unit cell size or electron mean free path. In general this condition is satisfied up to the UV region, $\lambda \gtrsim 100$ nm. Since we will study the optical properties of the samples in the near-infrared (NIR), visible (VIS) and ultraviolet (UV) spectral regions, we can consider this condition satisfied.

We define the *refractive index*

$$\tilde{n}(\omega) = \sqrt{\varepsilon(\omega)} \tag{1.6}$$

In general ε is a complex function of the angular frequency ω, which is a real number, and it can be expressed as $\varepsilon(\omega) = \varepsilon_1(\omega) + i\varepsilon_2(\omega)$, then the refractive index is a complex function too and it can be written as $\tilde{n}(\omega) = n(\omega) + ik(\omega)$.
The *extinction coefficient* $k(\omega) = \varepsilon_2/2n$, imaginary part of the refractive index, determines the optical absorption of EM waves propagating inside the material.
It is possible to connect $k(\omega)$ to the *absorption coefficient* α in the Lambert-Beer's law. This law describes the exponential attenuation of the beam intensity propagating through the medium via $I(x) = I_0 e^{-\alpha x}$. Thus, the relation between α and k is given by

$$\alpha(\omega) = \frac{2k(\omega)\omega}{c} \tag{1.7}$$

where c is the light speed in vacuum.

1.1.1 Drude Model

We have already exposed the importance of the dielectric function $\varepsilon(\omega)$ that gives us interesting information about metal-radiation interaction.
We explain now a simple theoretical model to estimate this function. This model is called *free electron gas model* or *Drude model* from its author, Paul Karl Ludwig Drude.

To explain this model we suppose a free electron density moving through fixed lattice formed by positive ions. Such electrons are considered to be free particles by neglecting electron-electron and electron-core interactions. However, some aspects of the band structure can be incorporated into the *effective mass* m of each electron.
The motion of electrons into the metal is damped only via collisions with the ions that, in analogy with kinetic theory, can be introduced with a characteristic *collision frequency* $\gamma = \frac{1}{\tau}$, where τ is know as the *relaxation time* of the free electron gas.

By considering a driving electric field $\mathbf{E}$ over free electrons, their motion equation results

$$m\ddot{\mathbf{x}} + m\gamma\dot{\mathbf{x}} = -e\mathbf{E} \tag{1.8}$$

If it is assumed a harmonic time dependence of the electric field $\mathbf{E}(t) = \mathbf{E}_0 e^{-i\omega t}$, it is possible to find the dielectric function in Drude model as

$$\varepsilon(\omega) = \varepsilon_\infty - \frac{\omega_p^2}{\omega^2 + \gamma^2} \; + \; i\,\frac{\omega_p^2\gamma}{\omega(\omega^2 + \gamma^2)} = \varepsilon_1(\omega) + i\varepsilon_2(\omega) \tag{1.9}$$

where $\omega_p = \sqrt{\frac{n\,e^2}{m\varepsilon_0}}$ is the *plasma frequency*, n is the *free electron density* and ε_∞ is a free parameter which varies between 1 and 10. In particular, ε_∞ takes into account

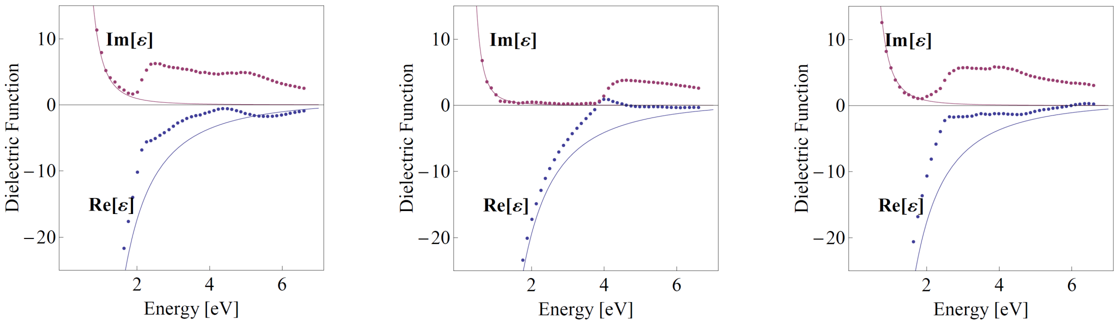

(a) Copper **(b)** Silver **(c)** Gold

Figure 1.1: Comparison of best fits, with Drude model (continuous line) and Johnson and Christy[21] (dots) for copper **(a)**, silver **(b)** and gold **(c)**.

the presence of a highly polarized environment caused by d electrons near the Fermi surface.

In Figure 1.1, the comparison between experimental data, from Johnson and Christy [21], and the best fits made with the analytical expression (1.9), is shown for three noble metals. We can notice that the model fails in reproducing the experimental data at the energies at which interband transitions becomes important. Specifically, for copper and gold this occurs at about 2 eV ($\sim$ 600 nm in wavelength) for silver at about 4 eV ($\sim$ 300 nm).

1.1.2 Drude-Lorentz Model

The Drude model was extended by Lorentz in order to overcome the disagreement found at energies higher than 2 eV where interband transitions become important. To overcome this limitation, Lorentz takes into account the contribution of bounded electrons, adding a harmonic term to the motion equation (1.8) which becomes

$$m\ddot{\mathbf{x}} + m\gamma\dot{\mathbf{x}} + m\omega_0^2\mathbf{x} = -e\mathbf{E} \tag{1.10}$$

ω_0 represents a resonance frequency that corresponds to a particular interband transition with $\hbar\omega_0$ energy.

When we consider more than one transition, we will have a system with the same number of non-homogeneous differential equations like (1.10), each of them with its own resonance frequency ω_j and collision frequency γ_j. Then, the dielectric function in this revised model results

$$\varepsilon(\omega) = \varepsilon_\infty - \frac{\omega_p^2}{\omega^2 + i\gamma\omega} + \sum_{j=1}^{N} \frac{A_j}{\omega_j^2 - \omega^2 + i\gamma_j\omega} \tag{1.11}$$

where A_j are free parameters which change depending on the considered metal.

Figure 1.2 shows a comparison between the experimental data from Johnson and Christy and the analytical dielectric function $\varepsilon(\omega)$, determined with the Drude-Lorentz model, performed by Hao and Nordlander [22] considering 4 interband transitions. It shows an excellent agreement with the experimental data. This is an interesting result for numerical calculation, thanks to the computationally simple formula of $\varepsilon(\omega)$.

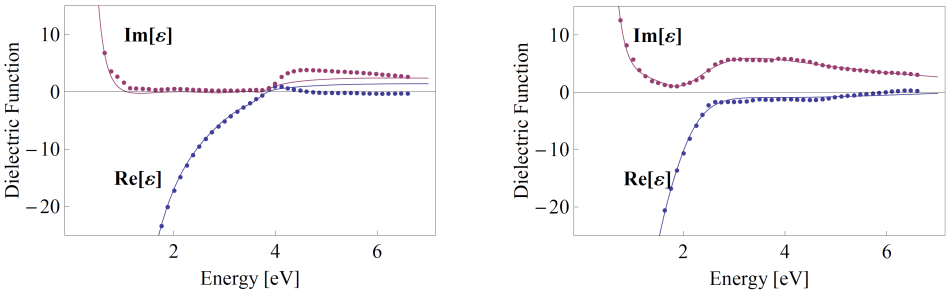

(**a**) Silver (**b**) Gold

Figure 1.2: Best fits to the experimental data from Johnson and Christy obtained with the Drude-Lorentz model, for silver (**a**) and gold (**b**).

1.2 Plasmon Polaritons

Plasmon is a quantum of free electron gas density oscillations. It can be consider as a quasiparticle from the quantization of plasma oscillations. We can distinguish three types of plasmons: *volume plasmon*, that occurs in a bulk metal; *surface plasmon*, that arises at an extended interface between a metal and a dielectric; *localized surface plasmon*, that arises at a confined interface between a metal and the dielectric.

1.2.1 Volume Plasmon

In the limit of high frequency, i.e., $\omega > \omega_p \gg \gamma$, metals are transparent to radiation and interband transitions can be neglected too. In this condition the real part of the dielectric function, $\varepsilon_1(\omega)$, prevails over the imaginary part, $\varepsilon_2(\omega)$, and we have

$$\varepsilon(\omega) \sim \varepsilon_1(\omega) = 1 - \frac{\omega_p^2}{\omega^2} \tag{1.12}$$

In this case metals support travelling waves. Therefore combining Maxwell's equations (1.1c) and (1.1d), where $\mathbf{J_{ext}}$ is assumed null, and assuming the dielectric function in the form (1.12) we can find the waves equation

$$\nabla^2 \mathbf{E} - \frac{\varepsilon}{c^2} \frac{\partial^2 \mathbf{E}}{\partial t^2} = 0 \tag{1.13}$$

Searching for a planar wave solution $\mathbf{E} = \mathbf{E}_0 e^{i(\mathbf{k}\cdot\mathbf{r} - \omega t)}$ one arrives at the Helmholtz equation $\nabla^2 \mathbf{E} + K^2 \mathbf{E} = 0$ with $K^2 = K_0^2 \varepsilon$ for which we can find the *dispersion relation*:

$$\omega^2 = \omega_p^2 + K^2 c^2 \tag{1.14}$$

In the long wavelength limit ($|\mathbf{K}| \to 0$), these travelling waves can be thought as collective oscillations of the electrons against the fixed ions, with frequency ω_p. The quanta of these oscillations are called *volume plasmons*. Since volume plasmons result uncoupled to EM radiation for their longitudinal nature, the only way of getting excited is by the impact of charged particles.

1.2.2 Surface Plasmon Polariton

Surface plasmon polaritons (SPP) are EM excitations which propagate at the interface between a metal and a dielectric and they are evanescently confined in a sub-wavelength spatial region in the perpendicular direction. The interesting point is that these EM surface waves arise via coupling of the free electron gas in the metal to EM field. If these plasmons occur at a surface with three-dimensional confinement, as nanoparticles, they are called *Localized Surface Plasmons* (LSP), which will be introduced in section 1.2.3.

We consider the wave equation (1.13) and we assume that the dielectric function $\varepsilon(\mathbf{r}, t)$ is independent of time and its variation over distances of the order of the optical wavelength is negligible. In addition, we consider a harmonic time dependence for the electric field $\mathbf{E}(\mathbf{r}, t) = \mathbf{E}(\mathbf{r})e^{-i\omega t}$ and we define $k_0 = \omega/c$ the wave vector in the vacuum. The propagation geometry for this problem is shown in Figure 1.3: wave propagation along x-direction, while the dielectric function depends only on the z coordinate, $\varepsilon(z)$; the planar interface between the dielectric medium and the metal is assumed to be at $z = 0$. Under this condition the Helmholtz equation can be written as

$$\frac{\partial^2 \mathbf{E}(z)}{\partial z^2} + (k_0^2 \varepsilon - \beta^2)\mathbf{E} = 0 \tag{1.15}$$

Where β describes the wave vector component along the propagation direction k_x and is called *propagation constant*. A similar equation can be deduced for the magnetic field $\mathbf{H}$.

Resolving eq. 1.15 (together with the similar one for $\mathbf{H}$) and imposing proper boundary conditions for the fields, the dispersion relations of a SPP results

$$\beta = k_0 \sqrt{\frac{\varepsilon\, \varepsilon_m}{\varepsilon + \varepsilon_m}} \tag{1.16}$$

where ε_m is the dielectric function of the dielectric medium and ε that of the metal.

We show in Figure 1.4, the dispersion relation at two interfaces, silver/air (gray curve) and silver/silica (black curve). Figure 1.4a is the plot of equation (1.16) for a metal described by Drude model in the limit of negligible damping, where the real part (continuous curve) and the imaginary part (dashed curve) of the wave vector β are shown. For large wave vectors ω tends to a characteristic value $\omega_{sp} = \frac{\omega_p}{\sqrt{1+\varepsilon_m}}$, called *surface plasmon frequency*. Figure 1.4b consider the experimental data by Johnson and Christy [21] for the Ag dielectric function.

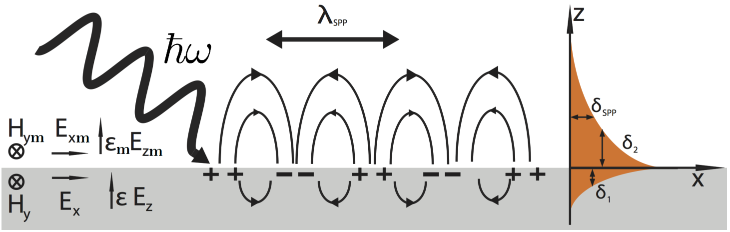

Figure 1.3: Geometry for SPP propagation at the interface between a metal and a dielectric. Electric and magnetic fields are also described.

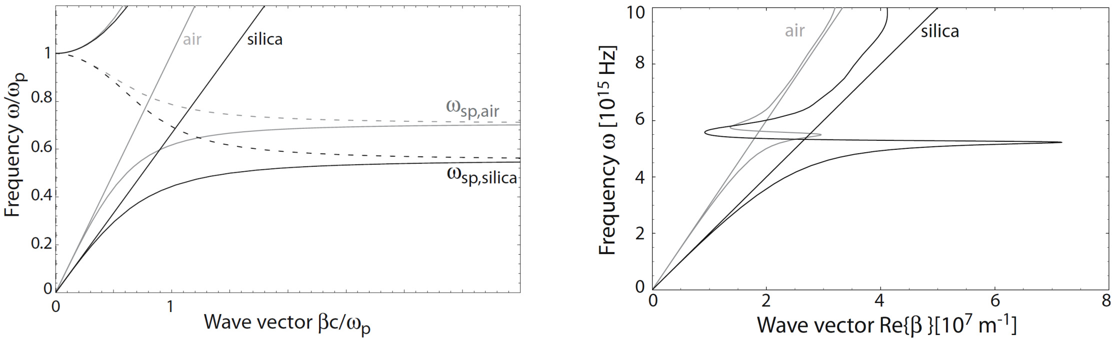

(a) Drude model for ε.

(b) Experimental data obtained by Johnson and Christy [21] for ε.

Figure 1.4: Dispersion relation of SSPs at silver/air (gray curve) and silver/silica (black curve) interface, for different estimations of the dielectric function.

To excite SPP, shining light is not sufficient, but phase-matching is required. Due to their bound nature, the SPP excitations correspond to the part of the dispersion curves, how we can see in Figure 1.4, lying to the right of the respective light lines for air and silica. Thus, special phase-matching techniques such as grating or prism coupling are required for their excitation.

1.2.3 Localized Surface Plasmon

Localized surface plasmons arise when we are in presence of nanoparticles that have three confined dimensions smaller than incident radiation wavelength. These plasmons are non-propagating due to their confined nature.

The electric field of the incident EM wave induces the motion of the electron cloud of the particle, as shown in Figure 1.5, altering the charge distribution. The presence of a restoring force induced by the depolarization field causes the system to behave like a forced-damped harmonic oscillator. When the exciting frequency is the correct one, the phenomenon of resonance called *localized surface plasmon resonance* (LSPR) arises. When this happens the electric field is amplified both inside and in the immediate vicinity (near-field zone) of the particle. This important effect is called *local field enhancement* and is the basis of all applications of plasmonic nanostructures in devices

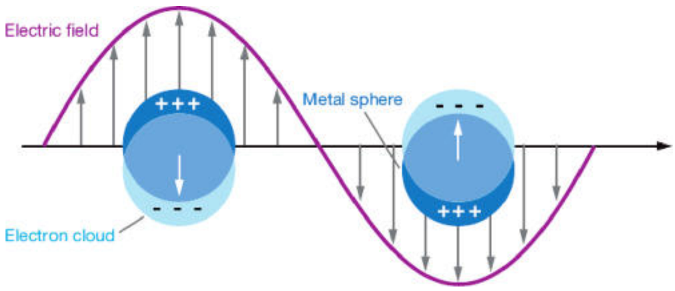

Figure 1.5: Schematic representation of the electrical induction of electron cloud oscillation in a metal particle made by an EM wave.

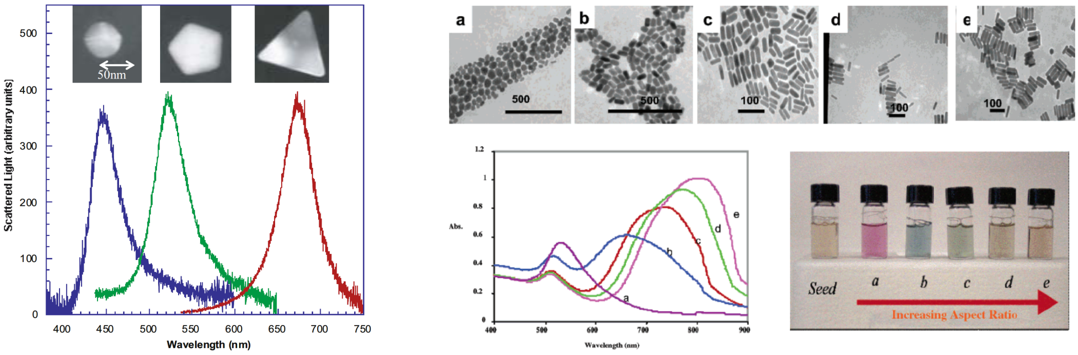

(a) (b)

Figure 1.6: **(a)** The extinction spectrum of three silver nanostructures with different shape in aqueous solution is shown and the inset shows images made by transmission electron microscopy (TEM) of the nanostructures in dark-field configuration [23]. **(b)** TEM images, optical spectra and photos of different aspect ratio gold nanorods in aqueous solution are shown [24].

or optical sensors.

Another important property of LSPs is the coupling with light. While SPPs need phase-matching by special coupling configurations, LSPs can be excited with direct radiation.

The LSP resonance depends on many factors as shape, size, electron density, electron effective mass, which characterise the nanoparticles and the dielectric function of media where the particles are immersed.

We can note from the images in Figure 1.6 how the different shape and size of the nanostructures alter the spectral position of the plasmon peak. In **(a)** it is shown the extinction spectrum of three silver nanostructures (TEM measurements in the inset) with different shape in aqueous solution [23]. In **(b)** TEM images, optical spectra and photos of different aspect ratio gold nanorods in aqueous solution are shown [24].

However, all these dependences make difficult an analytical approach. Only for spherical or spheroidal particles an analytical solution was obtained. For a spherical particle it will be discussed in the next section 1.3 in order to better understand this phenomenon. To this regard, Mie theory gives a full treatise of scattering and absorption of single non-interacting spherical particles [25–27] in a non-absorbing medium and a generalisation was made by Gans [28] for spheroidal particles. Out of this conditions, that is, for different shapes or interacting particles, numerical approaches are required due to problem complexity.

1.3 One Spherical Particle

A full approach for spherical nanoparticles with dielectric function $\varepsilon(\omega)$ in an environment with dielectric constant ε_m and an incident EM radiation with wavelength λ was developed by Mie in 1908 [25] and it is known as *Mie theory*.

In the following the results of Mie theory in the *quasi-static approximation* will be

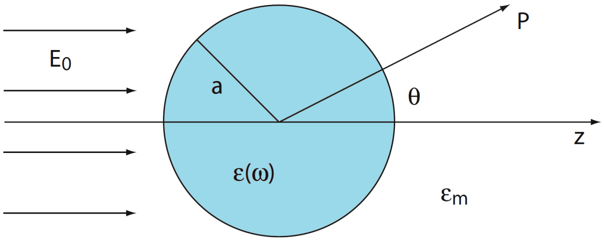

Figure 1.7: Geometry description for quasi-static approximation

presented. This approximation is strictly valid for sub-wavelength nanospheres, but it can be considered a good approximation in the visible or near-infrared region for spherical or ellipsoidal particles with dimensions up to tens of nanometers.

As mentioned before this approximation is strictly valid for particles of radius $a \ll \lambda$, where λ is the wavelength of incident radiation in the surrounding medium. In this condition, instantaneously, the particle perceives the electric field of radiation practically constant over its volume. Therefore we can simplify the problem considering a particle in an electrostatic field.

We define a convenient geometry for the analytical treatise, as shown in Figure 1.7. A homogeneous and isotropic sphere of radius a is placed at the origin in an isotropic and non-absorbing environment with dielectric constant ε_m. The dielectric response of the sphere is described via the dielectric function $\varepsilon(\omega)$. The sphere is immersed in a static electric field $\mathbf{E} = E_0\widehat{\mathbf{z}}$ along the $\mathbf{z}$ direction.

To calculate the electric field we can use the relation $\mathbf{E} = -\nabla\Phi$, where Φ is the electric potential. Φ can be determined by solving the *Laplace equation* that, in an electrostatic approach, results to be $\nabla^2\Phi = 0$.
Under these conditions, we can find the electric field inside and outside the spherical particles as

$$\mathbf{E_{in}} = \frac{3\varepsilon_m}{\varepsilon + 2\varepsilon_m}\,\mathbf{E_0} \tag{1.17a}$$

$$\mathbf{E_{out}} = \mathbf{E_0} + \frac{3\mathbf{n}(\mathbf{n}\cdot\mathbf{p}) - \mathbf{p}}{4\pi\varepsilon_0\varepsilon_m}\,\frac{1}{r^3} \tag{1.17b}$$

Where $\mathbf{n}$ is the unit vector in direction of the point of interest P (Fig. 1.7) perpendicular to the sphere surface and the dipole momentum $\mathbf{p}$ in this case is defined via [5]

$$\mathbf{p} = 4\pi\varepsilon_0\varepsilon_m a^3\,\frac{\varepsilon - \varepsilon_m}{\varepsilon + 2\varepsilon_m}\,\mathbf{E_0} \tag{1.18}$$

Furthermore, we can define the *polarizability* α via $\mathbf{p} = \varepsilon_0\varepsilon_m\,\alpha\,\mathbf{E_0}$ and thus in quasi-static approximation it is written as

$$\alpha_{qs} = 4\pi a^3\,\frac{\varepsilon - \varepsilon_m}{\varepsilon + 2\varepsilon_m} \tag{1.19}$$

If we consider a metal sphere with dielectric function $\varepsilon(\omega)$ described by Drude model and with slowly varying imaginary part, $Im[\varepsilon(\omega)]$, it is easy to find that a maximum of polarizability occurs when

$$Re[\varepsilon(\omega)] = -2\varepsilon_m \tag{1.20}$$

This condition is known as the *Fröhlich condition* and it is associated to a resonant mode of polarizability called *dipole surface plasmon* or *Localized Surface Plasmon Resonance* (LSPR). For a sphere immersed in air the Fröhlich criterion is satisfied at frequency $\omega_{LSPR} = \omega_p/\sqrt{3}$, assuming the high-frequency approximation of the Drude dielectric function.

We note that the resonance mode in α implies an enhancement of both internal and external dipolar fields. Outside the sphere the field decreases quickly, as r^{-3}, determining the properties in the *near-field* zone. For the internal field, we can define the *local field factor*, f, via $\mathbf{E_{in}} = f\,\mathbf{E_0}$ which identifies the enhancement factor inside the sphere.
These field enhancements at the plasmon resonance underlie fascinating and promising applications of metal nanoparticles in optical and sensors research.

If we introduce a harmonic time dependence for the electric field $\mathbf{E}(\mathbf{r},t) = \mathbf{E_0}e^{-i\omega t}$, then an oscillation of dipole momentum for $\mathbf{p}(t) = \varepsilon_0\varepsilon_m\alpha\mathbf{E_0}e^{-i\omega t}$ is induced, with α begin the same as for electrostatic treatise (eq. 1.19).

Complete electric and magnetic fields in presence of an oscillating electric dipole can be written [29] as

$$\mathbf{E_{dip}} = \frac{1}{4\pi\varepsilon_0\varepsilon_m}\left\{k^2(\mathbf{n}\times\mathbf{p})\times\mathbf{n}\,\frac{e^{ikr}}{r} + [3\mathbf{n}(\mathbf{n}\cdot\mathbf{p}) - \mathbf{p}]\left(\frac{1}{r^3} - \frac{ik}{r^2}\right)e^{ikr}\right\} \tag{1.21a}$$

$$\mathbf{H_{dip}} = \frac{ck^2}{4\pi}\,(\mathbf{n}\times\mathbf{p})\,\frac{e^{ikr}}{r}\left(1 - \frac{1}{ikr}\right) \tag{1.21b}$$

where $k = 2\pi/\lambda$ is the wavevector.

Interesting parameters, in particular for optical applications, are the cross sections for scattering σ_{sca} and absorption σ_{abs}. They can be calculated via *Poynting vector* ($\mathbf{S} = \frac{1}{\mu_0}\mathbf{E}\times\mathbf{H}$) with electric and magnetic fields from equations (1.21) and are linked to the polarization α by following equations:

$$\sigma_{sca} = \frac{k^4}{6\pi}\,|\alpha|^2 = \frac{8\pi}{3}\,k^4a^6\left|\frac{\varepsilon - \varepsilon_m}{\varepsilon + 2\varepsilon_m}\right|^2 \tag{1.22a}$$

$$\sigma_{abs} = k\,\mathrm{Im}[\alpha] = 4\pi k a^3\,\mathrm{Im}\left[\frac{\varepsilon - \varepsilon_m}{\varepsilon + 2\varepsilon_m}\right] \tag{1.22b}$$

So, we are now able to write the explicit expression of *extinction cross section* for a sphere of volume V and dielectric function $\varepsilon = \varepsilon_1 + i\varepsilon_2$ in quasi-static approximation as

$$\sigma_{ext} = \sigma_{sca} + \sigma_{abs} = 9\,\frac{\omega}{c}\,\varepsilon_m^{3/2}\,V\,\frac{\varepsilon_2}{[\varepsilon_1 + 2\varepsilon_m]^2 + \varepsilon_2^2} \tag{1.23}$$

Finally we can note that no restriction on the sphere's material was assumed, thus these expressions are still valid also for a dielectric sphere, even if in this case there is no resonance in the Fröhlich condition.

In Figure 1.8a it is possible to note the extinction cross sections, calculated using equation (1.23) in quasi-static approximation, of a silver nanosphere immersed in air (black squares) and silica (gray points). In particular, in Figure 1.8a, we can note the

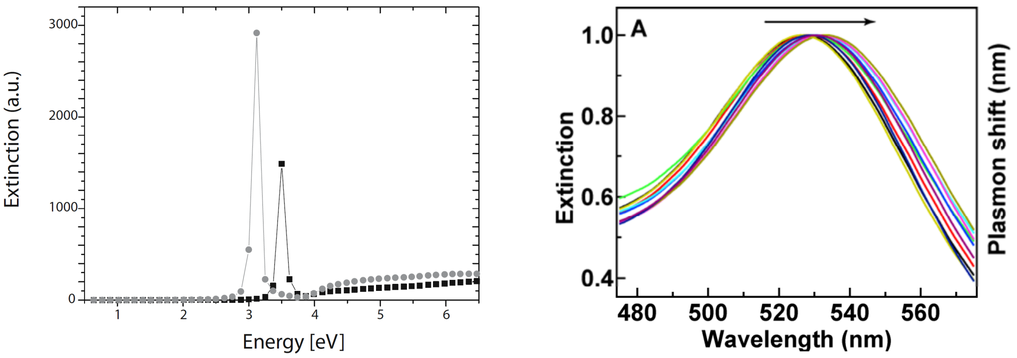

(a) Extinction cross section for a silver nanosphere in silica (gray) and air (black), calculated using equation (1.23). The Ag dielectric function is taken from Johnson and Christy [21].

(b) Normalized extinction spectra of gold nanospheres dispersed in a solution of water and glycerol in variable ratios. The arrow shows the direction in which the rate of glycerol increases [30].

Figure 1.8

shift of the LSPR wavelength due to the change of the dielectric refractive index in which the nanoparticle is immersed. In equation (1.23) it can be noted the dependence on the environment dielectric constant ε_m. This may be also experimentally verified as it can be seen in Figure 1.8b. The experiment conducted by Chen and co-workers [30] (Fig. 1.8b) shows that for gold nanospheres immersed in a solution of water and glycerol in variable ratios (i.e., with different dielectric constant) the LSPR peak is shifted to longer wavelengths by increasing the refractive index. This shift effect has many applications such as in optical sensing.

An extension of the quasi-static approximation was done in the *modified long-wavelength approximation* (MLWA), which extends the validity for larger particles. This approach performs a linear expansion over ka, called *size parameter* [31], where k is the wave vector and a is the sphere radius. Then, by using the expression (1.19) for one polarizability in the quasi-static approximation, the polarizability in MLWA can be determined [32] as

$$\alpha_{MLWA} = \frac{\alpha_{qs}}{1 - \frac{k^2}{a}\alpha_{qs} - \frac{2}{3}ik^3\alpha_{qs}} \tag{1.24}$$

We note two new terms at the denominator, each one with different physical significance. The first one, proportional to the square of the amplitude of the wave vector k, accounts for the effect called *dynamic depolarization* [31]. This describes the effect of the electric field produced by the charge distribution in one side of the particle delayed with respect to that other side. Depolarization field induces also an enhancement of polarizability, but other terms counteract this increase. The second term, purely imaginary, is related to radiative relaxation, called also *radiation damping*, that is essentially a direct decay way of a plasmon into a photon [33].

1.4 Many Nanoparticles

When we have more then one single nanoparticle and interaction among them is no longer negligible, the problem becomes very difficult to solve. The first approach was done by Maxwell and Garnett [34], who suggested an effective medium theory to describe a composite material as a homogeneous system with an effective dielectric function ε_{eff}, determined by the relation

$$\frac{\varepsilon_{eff} - \varepsilon_m}{\varepsilon_{eff} + 2\varepsilon_m} = p\,\frac{\varepsilon - \varepsilon_m}{\varepsilon + 2\varepsilon_m} \tag{1.25}$$

where ε_m and ε are the dielectric function of surrounding environment and metal nanoparticles, respectively, and p is the *filling factor*, that is the fraction of volume occupied by the nanoparticles. This theory, however, is a good approximation only for small particles ($a \lesssim 10$ nm) which can be described as dipoles and for small filling factors ($p \ll 1$).

If the particles are perfect spheres we can use another approach considering multipolar expansion: the *Generalized Multiparticles Mie Theory* (GMM) [35]. This result is often used in computation problem solving.

If instead we consider a system of nanoparticles with a long range order, new and interesting properties can appear. This type of system falls in a category called *photonic crystal.*

1.4.1 Photonic Crystals

Photonic crystals are in general periodic arrangements of nanostructures and their periodic dielectric function change the motion of photons, similarly to what happens with electrons in a ionic lattice.

The optical modes in a photonic crystal are calculated by the resolution of the Maxwell equations (1.1) in a periodic dielectric medium. However, an analytical solution is only possible for the one-dimensional case, while for two- or three-dimensional photonic crystals computational methods are required. Anyway, the one-dimensional solution gives us a lot of information about the phenomena that occur in multiple dimensions.

We can consider a one-dimensional photonic crystal as shown in Figure 1.9a: there are infinite planar layers with thickness d; the normal to each plane is along to the z direction; layer materials are non-magnetic, i.e., $\mu_1 = \mu_2 = 1$, and lossless; and the dielectric constant of the layers is assumed alternating between values ε_1 and ε_2.
There are two types of modes which are possible to distinguish: TE modes, in which the electric field is always in the plane of the layers, i.e., $\widehat{xy}$ plane and TM modes, in which the magnetic field is always in the $\widehat{xy}$ plane.

In order to solve Maxwell's equations we have to apply the boundary conditions at the interface between the adjacent layers and use the to Floquet–Bloch theorem [36, 37]. In the presence of a periodic medium we can apply this theorem, which states that an electric field in a periodic medium satisfies the relation

$$E(z + 2d) = e^{ik_B 2d} E(z) \tag{1.26}$$

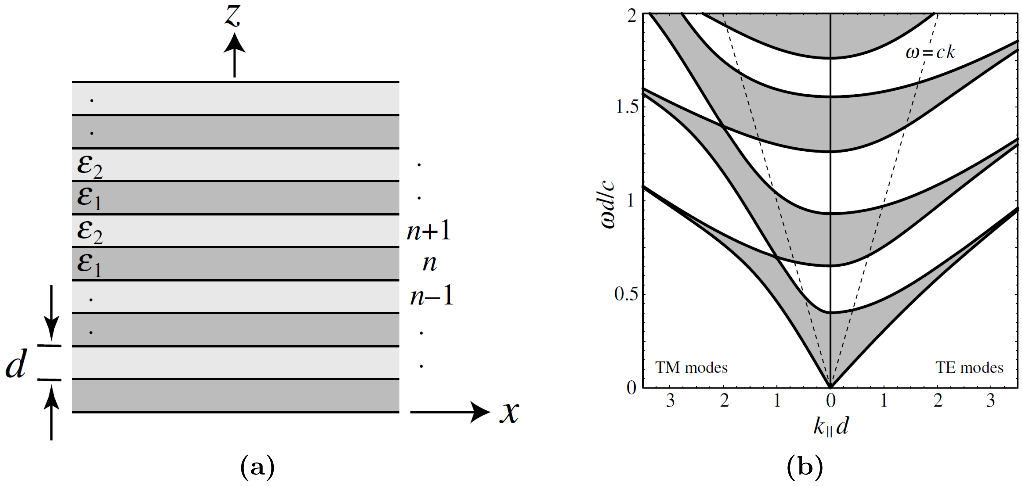

Figure 1.9: One-dimensional photonic crystal made of alternating layers of silica ($\varepsilon_1 = 2.33$) and InSb ($\varepsilon_2 = 17.88$): **(a)** schematic representation; **(b)** band diagram where the shaded areas are the allowed bands. [19]

where k_B is called *Bloch wavevector* and $2d$ is the periodicity of the system. For the magnetic field $H(z)$ there is a similar equation.

Then we can obtain the *characteristic equation*

$$\cos(2k_B d) = \cos(k_{z_1}d)\cos(k_{z_2}d) - \frac{1}{2}\left[p_m + \frac{1}{p_m}\right]\sin(k_{z_1}d)\sin(k_{z_2}d) \tag{1.27}$$

where $k_{z_j} = \sqrt{\varepsilon_j\,\omega^2/c^2 - k_{//}^2}$, the parallel wavenumber is defined as $k_{//} = \sqrt{k_x^2 + k_y^2}$ and p_m is a factor that depends on the polarization as $p_{TE} = k_{z_2}/k_{z_1}$ and $p_{TM} = k_{z_2}\varepsilon_1/k_{z_1}\varepsilon_2$.

The *band diagram* is the graph with all possible dispersion relations $\omega(k_{//})$ which is possible to find for each k_B. An example is shown in Figure 1.9b where both TE and TM modes are represented and the used values are $\varepsilon_1 = 2.33$ (SiO_2) and $\varepsilon_2 = 17.88$ (InSb). Furthermore, the shaded areas represent allowed bands where the propagation through the crystal is possible.

A wave propagating in vacuum has a dispersion relationship $\omega = ck$ which is represented in the band diagram in Figure 1.9b as dashed lines. Considering a wave propagating in vacuum impinging onto the photonic crystal, then it is possible to excite only modes with value of $k_{//}$ smaller than $k = \omega/c$. Therefore, since we can find complete bandgaps in the region $k_{//} < k$, for these frequencies, the photonic crystal results a perfect mirror.

1.4.2 2D Nanoparticles Array

In quasi-static or modified long-wavelength approximation the *coupled dipole method* (CDM) [38, 39] can be used to show how a periodic arrangement modifies the polarizability.

In order to understand the phenomena that can occur, we suppose an array with N spherical nanoparticles at positions $\mathbf{r}_i$ and with polarizabilities α_i described by equation (1.24) for more generality. The incident radiation induces a dipole momentum $\mathbf{p}_i = \varepsilon_0\varepsilon_m\alpha_i\,\mathbf{E_{inc}}_{,i}$ in each particle, as seen previously. But now we have to take into account also the relative retarded induced field $\mathbf{E_{dip}}_{,i}$ of the other $N-1$ dipoles. Then considering a local electric field $\mathbf{E_{loc}}_{,i}$ in each one, the dipole momenta become

$$\mathbf{p}_i = \varepsilon_0\varepsilon_m\alpha_i\,\mathbf{E_{loc}}_{,i} = \varepsilon_0\varepsilon_m\alpha_i(\mathbf{E_{inc}}_{,i} + \mathbf{E_{dip}}_{,i}) = \varepsilon_0\varepsilon_m\alpha_i(\mathbf{E}_0\,e^{i\mathbf{k}\cdot\mathbf{r}_i} - \sum_{\substack{j=1\\ j\neq i}}^{N} A_{ij}\cdot\mathbf{p}_j) \quad (1.28)$$

with i and j ranging from 1 to N. Here we have assumed the incident radiation in the form of a wave plane with amplitude $\mathbf{E}_0$ and wave vector $k = 2\pi/\lambda$. The dipole contribution $\mathbf{E_{dip}}_{,i}$ is built as the sum of each dipole interaction $A_{ij}\cdot\mathbf{p}_j$, where A_{ij} is called *dipole interaction matrix* [39]. Each term of $A_{ij}\cdot\mathbf{p}_j$ describes the electric field resulted from the interaction of two dipoles in $\mathbf{r}_i$ and $\mathbf{r}_j$, given by

$$A_{ij}\cdot\mathbf{p}_j = k^2\,e^{ikr_{ij}}\,\frac{\mathbf{r}_{ij}\times(\mathbf{r}_{ij}\times\mathbf{p}_j)}{r_{ij}^3} + e^{ikr_{ij}}\,(1-ikr_{ij})\,\frac{r_{ij}^2\mathbf{p}_j - 3\mathbf{r}_{ij}(\mathbf{r}_{ij}\cdot\mathbf{p}_j)}{r_{ij}^5} \quad (1.29)$$

with $(j \neq i)$ and where $\mathbf{r}_{ij}$ is the vector from i-particle to j-particle.

To obtain the polarization vectors we have to solve $3N$ linear equations of form the

$$A'\mathbf{p} = \varepsilon_0\varepsilon_m\mathbf{E} \quad (1.30)$$

where the diagonal terms of matrix are $A'_{ii} = 1/\alpha_i$ and the out of diagonal terms are the same as A_{ij} in equation (1.29).

For perpendicular incident radiation on the lattice plane and assuming an infinite array of elements and the same induced polarization for all particles, it is possible to obtain an analytical solution for the system of equations (1.30). In this way we have an expression for the modified polarizability of each particle

$$\alpha_{CDM} = \frac{1}{1/\alpha_{MLWA} - S} \quad (1.31)$$

where S is the *array factor* or retarded dipole sum that depends on particles separation and arrangement

$$S = \sum_{j\neq i}\left[\frac{(1-ikr_{ij})(3\cos^2\theta_{ij}-1)}{r_{ij}^3} + \frac{k^2\sin^2\theta_{ij}}{r_{ij}}\right]e^{ikr_{ij}} \quad (1.32)$$

where θ_{ij} is the angle between vector position $\mathbf{r}_{ij}$ and the polarization direction.
The total extinction cross section (eq.s 1.22-1.23) can be calculated as superimposition of the contributions of each particle, each one with polarizability α given by equation (1.31).

It can be noted that when

$$Re[1/\alpha_{MLWA}] = Re[S] \quad (1.33)$$

the polarizability has a maximum, which is associated to a resonant mode called plasmonic *Surface Lattice Resonance* (SLR).

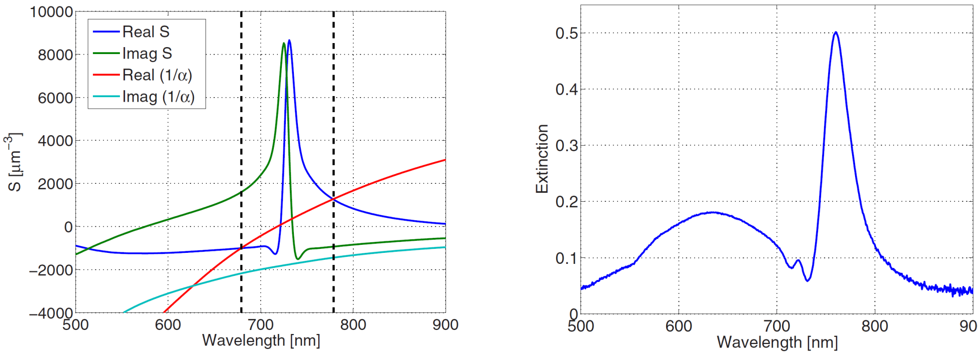

(a) (b)

Figure 1.10: **(a)** array factor for a hexagonal array (555 nm nearest neighbor separation) of silver disks (d = 120 nm, h = 30 nm); **(b)** Measured extinction. The array is index matched with $n = 1.515$, meaning that the diffraction edge is at 727 nm. Dashed lines in **(a)** indicate the intersection of the real parts of $1/\alpha$ and S. [40]

In Figure 1.10 an experiment conducted by Humphrey and Barnes [40] shows the agreement between the maximum condition (1.33) of equation (1.32) calculated numerically and the relative SLR peak in the extinction spectrum of a hexagonal array of spherical nanoparticles.

Chapter 2

Plasmonic NanoLaser System

In this chapter we will give a simple introduction to the concept of laser and the optical properties of the gain medium, one of the laser main component. More details can be found in many books such as those by Svelto [41], Siegmann [42], Silfvast [43], etc. In addition, to understand the lasing action from a nanolaser device the principal interactions between metallic nanostructures (discussed previously in the Chapter 1) and the gain medium (in the present case dye molecules) will be evaluated.

2.1 Laser Concepts

A LASER (*light amplification by stimulated emission of radiation* [6]) is a light source which is distinguished from the others by spatial and temporal coherence of emitted light, high monochromaticity and the ability to reach extremely high powers.

Typically a laser system is formed by three main parts: a *pump source*, a *gain medium* and an *optical resonant cavity*.

The pump is the part of the system that provides energy to the gain medium. Depending on the gain medium different types of pump schemes may be used. Pump sources commonly used are: flashlamps, light from another laser, electrical discharges and arc lamps.

The gain medium is the component in which the amplification of photons of *stimulated emission* occurs. Many types of materials can be used as a gain medium, the most common are: semiconductors, organic dyes, gases such as helium, neon, carbon dioxide or argon, and crystals or glasses appropriately doped with impurities such as chromium ions, neodymium, erbium or titanium.

The simplest optical resonator can be obtained by two mirrors between which it is placed the gain medium. One of these mirrors is high-reflective ($100\,\%$), while the other is semi-reflective ($\sim 95\,\%$) from which laser beam comes out. The configuration and arrangement of the mirrors constituting the optical cavity characterize the profile of the outgoing laser beam. The light emitted by the gain medium is reflected by the mirrors back into the medium, where it is amplified by *stimulated emission*. This feedback process strongly amplifies the light inside the cavity obtaining laser oscillations.

The theoretical foundations of the laser were established by Albert Einstein in 1917 [44], based on probability coefficients for *spontaneous emission*, *stimulated emis-*

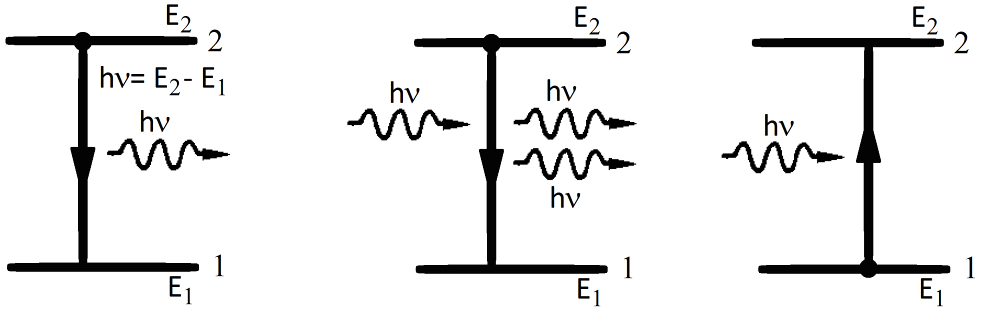

(a) Spontaneous Emission **(b)** Stimulated Emission **(c)** Absorption

Figure 2.1: Schematic representation of spontaneous emission, stimulated emission and absorption phenomena.

sion and *absorption* shown in Figure 2.1

2.1.1 Spontaneous Emission

We consider two energy levels of an atom or molecule, whose energies are E_1 and E_2 ($E_1 < E_2$). For simplicity we define the state E_1 as the ground state.

If we assume that the atom is initially in the state 2, it naturally tends to decay to the lower energy level E_1 (Fig. 2.1a). If this step is done by emission of an EM wave then the phenomenon is called *spontaneous* or *radiative emission*. For energy conservation, the emitted radiation will have energy equal to the difference of the two levels, $E_2 - E_1$, then a frequency ν_0 given by

$$\nu_0 = \frac{E_2 - E_1}{h} \tag{2.1}$$

where h is the Planck's constant.

If the decay process is not mediated by the emission of a photon, this is called *non-radiative* decay. In this case the energy $E_2 - E_1$ can go into kinetic or internal energy of the surrounding atoms or molecules.

We define N the population of a level, i.e., the number of atoms or molecules per unit volume that at time t are in a particular energy level. Regarding the spontaneous emission, the probability of the process is defined by the rate of decay of the upper state that is proportional to the population of the same state. In our case

$$\left(\frac{dN_2}{dt}\right)_{sp} = -AN_2 = -\frac{N_2}{\tau_{sp}} \tag{2.2}$$

where the positive constant A is called spontaneous emission rate or Einstein's coefficient for spontaneous emission A[1]. In addiction, we define the spontaneous emission lifetime $\tau_{sp} = 1/A$.

---

[1] Einstein was the first to give an expression for A by thermodynamic considerations.

Similarly, we can apply the same considerations for the non-radiative decay, and we can write

$$\left(\frac{dN_2}{dt}\right)_{nr} = -\frac{N_2}{\tau_{nr}} \tag{2.3}$$

with τ_{nr} the effective lifetime of the non-radiative decay process. Unlike τ_{sp} that depends only on the considered transition, τ_{nr} depends not only on the transition but also on the characteristics of the surrounding environment.

2.1.2 Stimulated Emission

We assume, as before, that the atom is initially at the excited level 2 and an EM wave with a frequency ν equal to that emitted in a spontaneous emission process, ν_0, impacts on the material into consideration. In this case there is a finite probability that the incident radiation forces the decay of the excited atom from the state 2 to 1 by emitting a photon which is added to the incident one. This process is called *stimulated emission* (Fig. 2.1b).

There is a substantial different between the photon emitted in this process and one created in a spontaneous emission process. In the spontaneous emission process the atom does not have a direction of preferred emission and the emitted EM wave does not have a definite phase in relation with the other EM waves emitted by surrounding atoms. In contrast, the photon emitted by a stimulated emission process has the same phase and is directed along the same direction of the incoming photon.

Regarding the decay rate we can write in a similar way to the spontaneous emission

$$\left(\frac{dN_2}{dt}\right)_{st} = -W_{21}N_2 \tag{2.4}$$

where the stimulated emission rate W_{21}, differently from the Einstein's coefficient A, depends on the particular transition and also on the flux F of incident photons as

$$W_{21} = \sigma_{21}F \tag{2.5}$$

where σ_{21} has the dimension of an area and is called *stimulated emission cross section*, which depends only on the considered transition.

2.1.3 Absorption

The phenomenon taken into account now is the *absorption*. This process can occur when an atom, assumed initially at the ground state, is stimulated by an EM wave. In the case in which the incident wave has a frequency $\nu = \nu_0$, then there is a finite probability that the atom is excited to the state 2 (Fig. 2.1c). The incident photon is then annihilated, transferring the energy for the atom excitation.

For this phenomenon the probability of absorption is given by

$$\left(\frac{dN_1}{dt}\right)_{a} = -W_{12}N_1 \tag{2.6}$$

where W_{12} is the absorption rate which in this case too depends on the flux of photons

$$W_{12} = \sigma_{12} F \tag{2.7}$$

where σ_{12} is the *absorption cross section* which depends only on the particular transition.

Furthermore, Einstein found that if the two levels are non-degenerate then $W_{21} = W_{12}$ and $\sigma_{21} = \sigma_{12}$. Otherwise $g_2 W_{21} = g_1 W_{12}$ and $g_2 \sigma_{21} = g_1 \sigma_{12}$ where g_1 and g_2 are the degenerate degrees of state 1 and 2, respectively.

In addiction, a well-known and useful parameter is *absorbance* defined as

$$A = -\log\left(\frac{I}{I_0}\right) \tag{2.8}$$

where I_0 and I are respectively the incident and transmitted intensities. Absorbance defines the *optical density* (OD) of the material and it is linked to the absorption coefficient α in the Lambert-Beer's law ($I = I_0 e^{-\alpha x}$) as

$$A = \alpha L \log e \tag{2.9}$$

where L is the optical path length inside the material.

The absorption coefficient α is related to the linear absorption cross section in equation (2.7) via

$$\alpha = \sigma_{12} N_1 \tag{2.10}$$

2.1.4 Rate Equations

We assume a photon flux which travels along the $\widehat{z}$ direction. The flux variation along $\widehat{z}$ will be given by the difference between stimulated emitted photons and absorbed ones

$$\frac{dF}{dz} = \sigma_{21} F [N_2 - (g_2 N_1 / g_1)] \tag{2.11}$$

Spontaneous emitted photons are emitted in all directions and then they would give a negligible contribution in $\widehat{z}$ direction.

We note that the outgoing flux is grater than incoming one when $N_2 > g_2 N_1 / g_1$. This condition is called *population inversion* and a material in this condition behaves as a gain medium. If instead $N_2 < g_2 N_1 / g_1$, then the material behaves as an absorber inasmuch the outgoing flux is lesser than the incoming one.

We consider a material at thermal equilibrium, then the population of the states can be described by Boltzmann statistics. Under these considerations the population ratio results

$$\frac{N_2^e}{N_1^e} = \frac{g_2}{g_1} e^{-\frac{E_2 - E_1}{k_B T}} \tag{2.12}$$

where $k_B = 1.38 \times 10^{-23}$ JK^{-1} is the Boltzmann constant and T is the temperature in Kelvin degrees.

We note that at thermal equilibrium a material is an absorber because $N_2 < g_2 N_1 / g_1$. Therefore, to reach the population inversion we must stimulate from the outside the

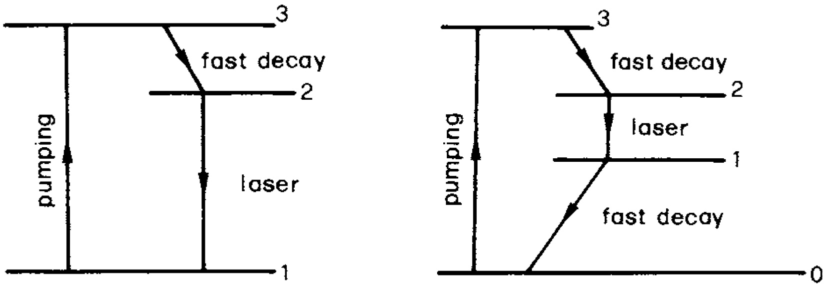

(a) Three-level scheme (b) Four-level scheme

Figure 2.2: Schematic representation of the three- and four-level systems for laser emission.

material, for example with an optical pumping process. At a certain point the system will be in a condition where $N_2 g_2 = N_1 g_1$. At this point the stimulated emission compensates the absorption and the material becomes transparent to the radiation. This condition is called two-level saturation and forbids the possibility to achieve population inversion if only two levels are involved in the process.

However, the population inversion can be achieved if one considers more than two levels. In Figure 2.2 schematic three- and four-level systems are shown. An important assumption is that τ_{31} and τ_{10} are both much smaller than the lifetime of the laser transition τ_{21}. In this way, N_3 and N_1 can be considered always $\simeq 0$, while N_2 increases and two-level saturation is avoided. Therefore, with a proper pumping flux, the population inversion can be reached between the states 1 and 2.
We note that in a four-level system the population inversion is easier to reach, because level 1 is already empty if it is far enough from the ground state ($E_1 - E_0 > k_B T$). Furthermore, if we assume that τ_{10} is very short, as may be a non-radiative process, the population inversion is also easier to maintain.

The dynamic of the populations as well as the photon flux can be evaluated by a simple model of rate equations. This model is based on the balance between the atom transitions and the number of the photons created or annihilated.
For a four-level system with non-degenerate levels we can write the system of rate equations as

$$\frac{dN_0(t)}{dt} = \frac{N_1(t)}{\tau_{10}} + \frac{N_3(t)}{\tau_{30}} - W_p\, N_0(t) \tag{2.13a}$$

$$\frac{dN_1(t)}{dt} = \frac{N_2(t)}{\tau_{21}} - \frac{N_1(t)}{\tau_{10}} - F\,\sigma_{21}\,[N_1(t) - N_2(t)] \tag{2.13b}$$

$$\frac{dN_2(t)}{dt} = \frac{N_3(t)}{\tau_{32}} - \frac{N_2(t)}{\tau_{21}} + F\,\sigma_{21}\,[N_1(t) - N_2(t)] \tag{2.13c}$$

$$\frac{dN_3(t)}{dt} = -\frac{N_3(t)}{\tau_{32}} - \frac{N_3(t)}{\tau_{30}} + W_p\, N_0(t) \tag{2.13d}$$

where W_p is a suitable rate describing the pumping process Moreover, it is supposed that $N_3 \ll N_0$ and the total population $N_t = N_0 + N_1 + N_2 + N_3$.

2.1.5 The Organic Laser Dye

In the present work the gain medium is an organic laser dye, named Styryl 9M (appendix A). The complex structure of this molecule makes a detailed analysis of its properties difficult. Anyway, it is possible to describe the molecules by the so-called *free electron model* [45], which considers the molecule as a potential well with its electrons inside. The energy diagram can be represented as a function of a configuration-coordinate[2] (Fig. 2.3a [46]).

In Figure 2.3a we can note the energy levels labelled with S_0 and S_1, which are the levels associated to the singlet state with total spin $S = 0$, and T_1 and T_2, which are the levels associated to the triplet state with total spin $S = 1$. Furthermore, it is possible to note the presence of sublevels due to the vibrational and rotational state of the molecule. These sublevels spread the spectrum of transitions, creating a bandwidth of about 100 nm as we can note in Figure 2.3b where the absorbance and emission spectra of Styryl 9M dissolved in ethanol are shown.

From selection laws we know that the transition with $\Delta S \neq 0$ are forbidden. This means that in our case the triplet-singlet transitions will have very long lifetimes ($\sim$ ms), while the singlet-singlet transitions lifetimes are around few ns. These transitions govern the fluorescence phenomenon of interest. Fluorescence is the emission of light by a material that has absorbed EM radiation. Moreover, the emitted light has a longer wavelength, and therefore lower energy, than the absorbed radiation. The shift between absorbed and emitted radiation wavelength is called Stoke's shift.

We can define the fluorescence *quantum yield* as the ratio of the number of photons emitted to the number of photons absorbed and it is possible to link it to the transition lifetimes as

$$\eta = \frac{\text{number of photons emitted}}{\text{number of photons absorbed}} = \frac{\tau_t}{\tau_r} \tag{2.14}$$

where τ_r is the radiative lifetime, while $\tau_t = \left[\sum_i 1/\tau_i\right]^{-1}$ with τ_i the lifetimes of all possible excited state decays.

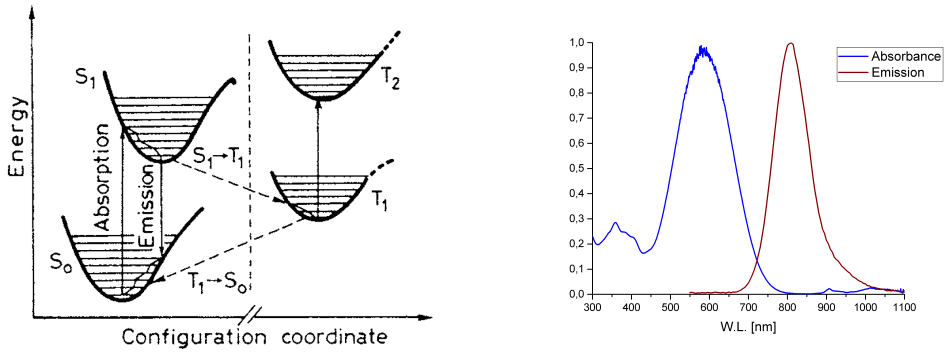

(a) (b)

Figure 2.3: The laser dye: **(a)** schematic representation of energy levels [46]; **(b)** example of the absorbance and fluorescence spectra (Styryl 9M in ethanol).

---

[2] a coordinate describing one of the many vibrational modes that a long-chain dye molecule has.

Bleaching

A phenomenon that affects the dye molecules to which we have to pay attention is *bleaching.* This phenomenon refers to the loss of the color due to the loss of interaction with the radiation in the visible range, and then the decrease of quantum yield. The bleaching is due to the environment in which the molecules are embedded, such as the solvent or the matrix that hosts them and the impurities that may be present in the surrounding environment.

In our case the main bleaching process is that of *photobleaching.* This occurs when the dye molecules are subjected to a relatively intense photon flux. The energy transferred by the photons can induce chemical reactions with the surrounding environment.

It was verified that this phenomenon is a one-photon process and occurs as the molecules are in singlet or triplet excited state [47]. Moreover, impurities such as oxygen present in the environment, due to the porosity of the matrix or from the polymerization process, are the main causes of photobleaching. In particular, a molecule that is in triplet excited state has many chances to interact with the surrounding environment due to its long lifetime, via for example the reaction $T_1 +^3 O_2 \rightarrow S_1 +^1 O_2$ [48, 49].

Regarding this work it is assessed a lifetime of photobleaching at different incident beam energy fluxes, evaluating a secure working condition by an excessive signal loss due to the photobleaching. The obtained results are presented in section 5.1.

2.2 Gain Medium and Metallic Nanostructures

To obtain a laser beam generally one puts the gain medium within a resonant optical cavity in order to obtain a laser oscillator, just as said before. The idea of a plasmonic nanolaser device is to replace the conventional cavity with a two-dimensional array of plasmonic nanostructures. Many interesting phenomena occur due to the interaction of metallic nanostructures with a gain medium. An important phenomenon is the interaction of the gain medium with the field confined by the nanoparticles in the near-field zone under resonant excitation. The gain medium coupled with the near-field plasmonic modes can have enough gain to compensate the losses inherent within the metal and then activate the lasing action.

The plasmonic nanolaser devices have recently been demonstrated. Among the pioneer research groups in this field it is that of T. Odom at the Northwestern University in Illinois. They have built some lasing band-edge devices which exhibit normal laser action to the surface. By electron beam lithography (EBL), they have synthesized different ordered nanostructures coupled with a laser dye as gain medium generally in liquid state [11–13].

On the other hand, in the same year F. Van Beijnum and collaborators have achieved a nanolaser device using a semiconductor coupled to a nanohole array [50]. However, in this experiment the device must be kept at temperatures down to 5 K to allow a laser emission. Later, in the same year, other research groups such as those of A. F. Koenderink at the research center AMOLF or B. T. Cunningam in Illinois, have synthesized and characterized plasmonic devices nanolaser [14, 15]. In these works it has proved the possibility of having laser emission from laser dyes coupled to plasmonic nanostructures ordered in quasiperiodic patterns or with a non-normal emission to the sample surface.

Regarding to the thoretical model to describe the lasing behaviour in plasmonic nanosystem, Dridi and Schatz in 2013 [8] have modelled the lasing emission phenomenon by dye molecules coupled with a periodic array of metallic nanostructures. Via a semi-classical treatment, the contribution of the amplified electric field associated to plasmonic modes is taken into account in the rate equations. In particular, the model considers the microscopic polarization of molecules induced by the optically pumped transitions. Then, the net macroscopic polarization is connected to the microscopic one by the variation of the population ΔN_{ij} of the energy levels involved in the transition, and not by the population N_i of a single level. Furthermore, it is taken into account the variation in time of $\Delta N_{ij}(t)$ in order to consider non-linear effects of spontaneous emission, stimulated emission and absorption.

The equation that describes the interaction of the EM field with the molecules of the gain medium can be written through the net macroscopic polarization of the gain medium as [42, 51]

$$\frac{d^2\mathbf{P}_{ij}(t)}{dt^2} + \Delta\omega_{ij}\,\frac{d\mathbf{P}_{ij}(t)}{dt} + \omega_{ij}^2\,\mathbf{P}_{ij}(t) = \frac{6\pi\varepsilon_0 c^3}{\omega_{ij}^2\gamma_{ij}}\,\Delta N_{ij}(t)\,\mathbf{E}(t) \tag{2.15}$$

Here ω_{ij} is the angular frequency, $\Delta\omega_{ij}$ is the bandwidth due to radiative, non-radiative and collision effects and γ_{ij} is the damping coefficient of a specific transition.
Consequently, the resulting macroscopic polarization acts on the electric field and tends to change it. This effect can be taken into account by including a current $\mathbf{J} = \partial\mathbf{P}/\partial t$ in the Maxwell's equations.

We consider a gain medium described by a four-level system, as shown in Figure 2.4.

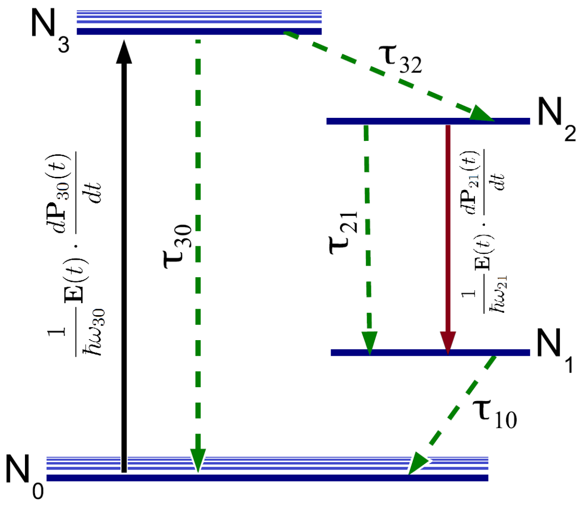

Figure 2.4: Four-level diagram to describe dye molecules: dashed arrows represent spontaneous transitions and continuous arrow are for stimulated processes.

We can then write the system of rate equations as [8]

$$\frac{dN_0(t)}{dt} = \frac{N_1(t)}{\tau_{10}} + \frac{N_3(t)}{\tau_{30}} - \frac{1}{\hbar\omega_{30}}\mathbf{E}(t) \cdot \frac{d\mathbf{P}_{30}(t)}{dt} \tag{2.16a}$$

$$\frac{dN_1(t)}{dt} = \frac{N_2(t)}{\tau_{21}} - \frac{N_1(t)}{\tau_{10}} - \frac{1}{\hbar\omega_{21}}\mathbf{E}(t) \cdot \frac{d\mathbf{P}_{21}(t)}{dt} \tag{2.16b}$$

$$\frac{dN_2(t)}{dt} = \frac{N_3(t)}{\tau_{32}} - \frac{N_2(t)}{\tau_{21}} + \frac{1}{\hbar\omega_{21}}\mathbf{E}(t) \cdot \frac{d\mathbf{P}_{21}(t)}{dt} \tag{2.16c}$$

$$\frac{dN_3(t)}{dt} = -\frac{N_3(t)}{\tau_{32}} - \frac{N_3(t)}{\tau_{30}} + \frac{1}{\hbar\omega_{30}}\mathbf{E}(t) \cdot \frac{d\mathbf{P}_{30}(t)}{dt} \tag{2.16d}$$

where the last term in the each rate equation identifies the energy transferred between the EM field and the gain medium molecules [42, 52–54]

The considered electric field $\mathbf{E}(t)$ identifies the total electric field. This takes into account the incident radiation and the one emitted by the gain medium, as well as the contribution of nanostructures. This field is calculated using the *finite-difference time-domain* (FDTD) numerical technique. Computational techniques for the electric field are needed, unless spherical or spheroidal nanostructures, as done in the work by Martikainen and co-workers [10].

2.2.1 Purcell Effect

Another effect that can occur is called the Purcell effect. This effect describes the modification of the radiative and non-radiative decay rate by the presence of a cavity.

As seen in Chapter 1, a nanoparticle acts as an optical resonator in the vicinity of its surface. So we expect that this effect arises again. Regarding to this phenomenon, Anger and co-workers have performed an interesting and explanatory work [55]. They have investigated the fluorescence rate of a single molecule as a function of its separation from a laser-irradiated spherical gold nanoparticle.

In this work two effects are emerged: the fluorescence amplification and quenching. Figure 2.5 shows the comparison between experiment (dots) and theory (solid curves), where the radiative rate γ_{em} value is normalized with their corresponding free-space value γ_{em}^0. The model takes in to account multiple multipole method [19] in order to consider the quenching effects, not predicted by the dipole approximation. As we can note in Figure 2.5, when the gold nanoparticle get close to the molecule, a phenomenon of fluorescence enhancement arises. This phenomenon is explained and modelled as the modification of the decay rate, in according to the Purcell effect. This modification is caused by the electric field, which is modified by the plasmonic modes of the nanostructure that act as an optical cavity.

But, when the nanoparticle get more close, a quenching phenomenon occurs. This quenching phenomenon is due to the non-radiative energy transfer that, for short distances, becomes important thereby quenching the fluorescence of the molecule. The principal contribute of this non-radiative energy transfer is due by Förster resonant energy transfer (FRET), that describes mechanism of energy transfer between donor molecules and metal surface instead of an organic acceptor. This effect of donor-acceptor match changes also the radiative rate of the molecules, modifying quantum efficiency η of the system.

From this experiment, we can note that dye molecules in the proximity of nanoparticles have a enhancement on the fluorescence emission. However, the molecules too close to the nanostructures present a drastically decrease of the quantum yield due to the quenching phenomenon. Regarding our system these phenomena can occur near to the pasmonic nanostructures and we have to take into account especially if one considers a dye-doped thin films.

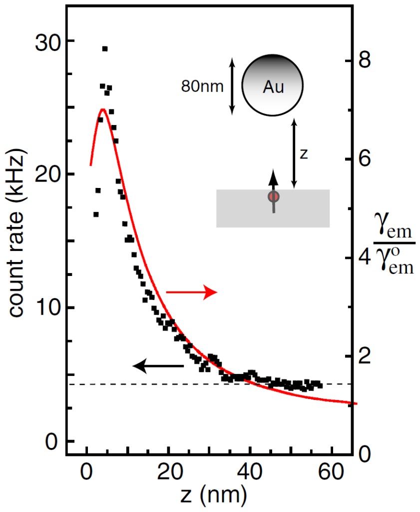

Figure 2.5: Experimental and theoretical results by Anger et al. [55]. The radiative rate γ_{em} value are normalized with their corresponding free-space value. The experiment (dots) and theory (solid curves) are compared and dashed line indicates background level.

Chapter 3

Samples Synthesis

The increasing interest toward the production of two-dimensional ordered arrays nanoparticles has led to several synthesis methods to obtain structures of higher and higher quality and of various typologies, and to get a better control over shape, size, chemical composition, inter-particles spacing, defects and surrounding environment of the nanostructures.

Among these methods, the most noteworthy ones are the techniques as *electron beam lithography* (EBL), *focused ion beam* (FIB) and *scanning probe microscopy* (SPM) *lithography*, thanks to which it is possible to have excellent precision on shape, size and degree of order of the nanostructures [56, 57]. Nonetheless, these techniques require expensive instruments and long fabrication time, reducing the working area down to mm^2. Other procedures to achieve larger nanostructured areas have been developd, but they need expensive facilities in any case, such as *x-ray lithography*, *laser interference lithography* or *nanoimprinting* [57–59].

Alternatively, a versatile and cost-effective technique, firstly proposed and systematically described by R. P. Van Duyne in 2001 [60], is the *nanosphere lithography* (NSL), which will be adopted in the present work.

This technique is based on the self-assembling of a monolayer, of size-mono-disperse

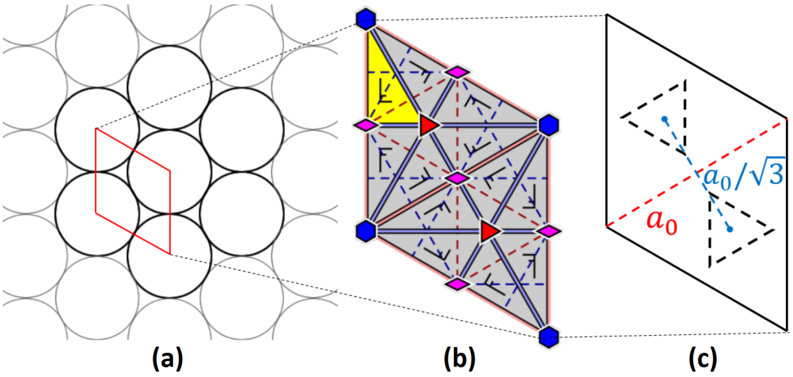

Figure 3.1: The lattice resulting from NSL: **(a)** a nanosphere together its 6 first neighbours, and the unit cell definition; **(b)** symmetries in the unit cell; **(c)** relevant parameters in the unit cell: the lattice parameter $a_0 = D$ (spheres' diameter) and the centre-centre distance $d = a_0/\sqrt{3}$.

polystyrene (PS) nanospheres (NS) whose diameter ranges from 40 nm to few μm. This spontaneous phenomenon of aggregation allows the formation of a two-dimensional hexagonal close-packed crystal (shown in figure 3.1) on the surface of a substrate, over areas up to some cm^2 and with defectless domains that reach areas of a hundred μm^2 [61].
In figure 3.1 it can be seen the unit cell of the hexagonal lattice highlighted in red above the pattern formed by the PS nanospheres, **(a)**. In **(b)** the respective symmetries of the unit cell are shown. Finally, the two characteristic values reported in **(c)** identify the grating period a_0, which in is equivalent to the PS nanospheres' diameter D, while the other one $d = a_0/\sqrt{3}$ represents the centre-centre distance that correspond to the distance between the interstices formed among the neighbouring spheres.

The polystyrene self-assembled manolayer acts as lithographic mask to create different two-dimensional ordered metallic nanostructure arrays. The structure chosen and optimized for this work is the *nanodome array*. It is manufactured as shown in figure 3.2 and all the passages will be described in detail in the following sections. Briefly, the PS mask undergoes a treatment of *reactive ion etching* (RIE) that reduces the spheres' size while maintaining the periodicity of the initial structure.
Later, a silica layer is deposited by magnetron sputtering to create a mechanically, chemically and physically more stable substrate, maintaining the dome geometry. The plasmonic nanostructure is then formed by deposition of a gold layer upon the silica one. The sample is completed with the deposition of dye-doped polymer film upon the gold nanostructures, by evaporating solvent of a solution with dye and monomers.

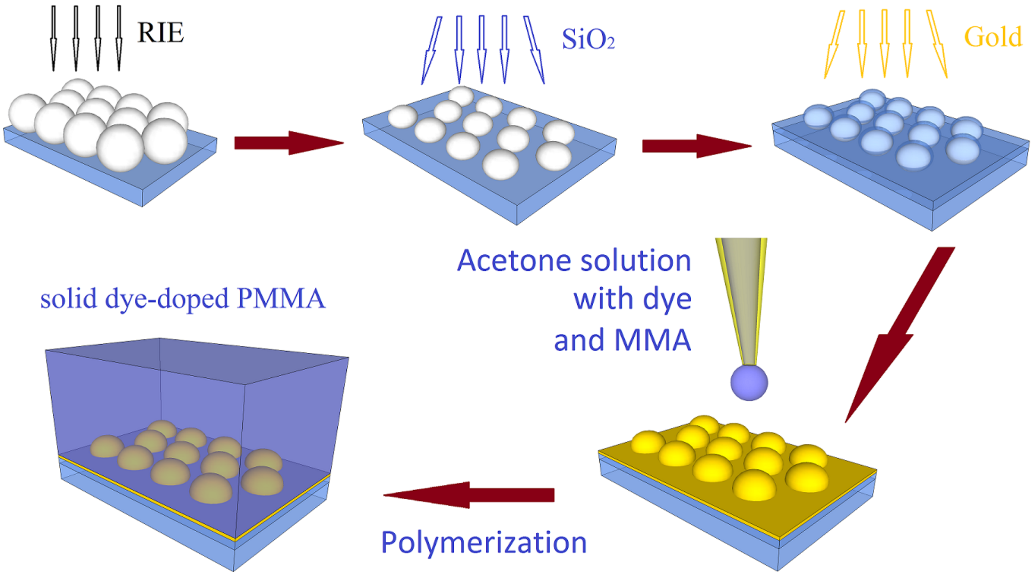

Figure 3.2: Schematic representation of the fabrication steps for the synthesis of the nanodome array. First, a close-packed array of PS nanospheres is formed by self-assembling. The RIE process is used to reduce the spheres' size. Silica and gold layers are then deposited upon PS NSs by magnetron sputtering. In the end a dye-doped film of PMMA is created on top of the nanostructures by solvent evaporation.

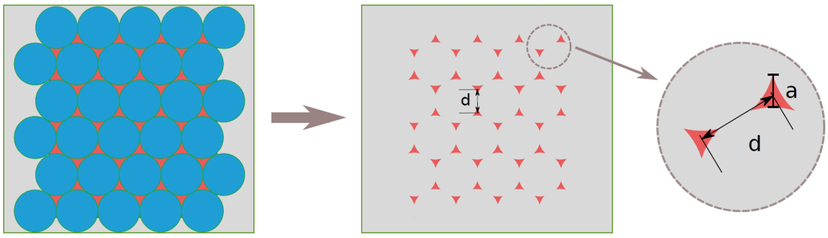

Figure 3.3: Triangular nanoprism array obtained by NSL. First, the metal is deposited (left) then the mask is removed (right).

Among the different nanostructure arrays which can be synthesized by NSL, another interesting type of nanoarray is the triangular *nanoprism array*. The high field enhancement that occurs between adjacent prism may be used for these devices.

The triangular nanoprism array is made by direct evaporation of metal on a PS mask, without RIE, and the successive removal of the PS mask (see figure 3.3). After that, the dye-doped polymer is deposed.

In the figure 3.3 we can see the honeycomb structure of the triangular nanoprisms. The distance between neighbour prisms will be equal to the interstitial distance of the PS nanospheres pattern, that is d= $D/\sqrt{3}$, where D is the nanospheres diameter. Moreover, it can be pointed out a relationship between the lateral in-plane dimension of the triangular base a and the NS's diameter

$$a = \frac{3}{2}\left(\sqrt{3} - 1 - \frac{1}{\sqrt{3}}\right) a_0 \approx 0.233\, D \tag{3.1}$$

This shows how the geometrical dimensions of the desired nanostructure can be tuned by properly choosing the initial nanospheres' diameter.

3.1 Polystyrene Mask Formation

3.1.1 Self-assembling

Before assembling the PS mask on the substrates, these have to be cleaned and made hydrophilic in order to reduce, as far as possible, the formation of defects in the crystal. Three types of substrate have been used with an area of some cm^2: Soda Lime Glass (SLG) is utilised only during mask formation; 1 mm thick, highly-pure silica (SiO_2) (Heraeus HSQ300) pieces are the final substrate for the device; 0.4 mm thick monocrystalline silicon (Si), obtained from silicon wafers of Silicon Materials, is used for morphology characterizations by SEM (scanning electron microscopy).

The cleaning process is made by an *acid piranha* solution, which is composed of sulphuric acid (H_2SO_4) and hydrogen peroxide (H_2O_2) in proportion 3:1. The substrates are immersed in this solution and left for one hour at 90 °C. This strong oxidising process guarantees the removal of most organic matter impurities from the surfaces which are made simultaneously hydrophilic.

After that, the substrates are widely rinsed with Milli-Q water (18.2 MΩ/cm resistivity at 25 °C) and then immersed, for 20 minutes at 90 °C, in a basic 3:1 solution, called

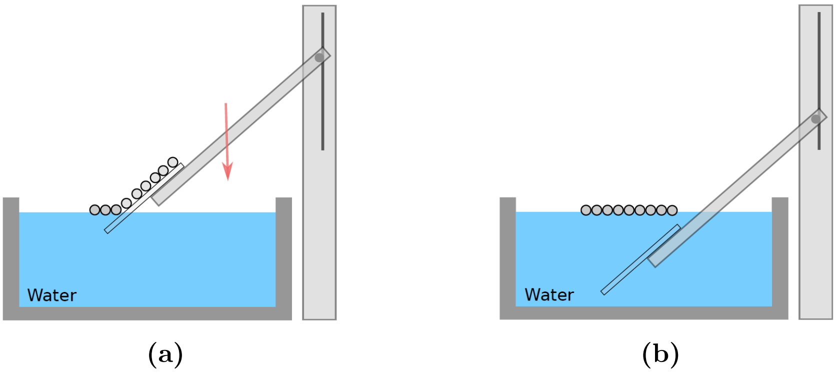

Figure 3.4: Schematic description of the device used for the mask self-assembling: the SLG substrate is fixed at the end of a motorized arm. PS nanospheres in colloidal solution are deposited on the glass. The glass is dipped in water **(a)** and the NSs float on the water surface **(b)** forming an ordered monolayer.

basic piranha, of ammonium hydroxide (NH_4OH) and hydrogen peroxide. This step adds a further level of cleaning and increases the surface hydrophilicity.

In this work, PS nanospheres with diameter $D = 522 \pm 12$ nm are used. They are produced by Microparticles GmbH and preserved in a colloidal watery solution at 5% in volume. The solution is equally mixed with alcohol (2-Propanol) to quicken the evaporation.

From the previously prepared solution, 25 μl are extracted and homogeneously distributed on a SLG substrate which is fixed on a motorized arm and positioned above a crystallizer filled with high-purity Milli-Q water. As shown in figure 3.4, the SLG is slowly lowered and almost completely immersed in water. During the descent, the PS spheres separate from the substrate and arrange them self on the water surface to form a monolayer, thanks to the meniscus between alcohol and water.

For spheres of the size used, an iridescent coloration appear due to interference on the monolayer and this action is accentuated in the ordered zones, making them recognisable. Then, the mask is picked up with SiO_2 or Si substrates (figure 3.5), and then left to dry in order to form the hexagonal close-packed ordered structure, thanks to solvent

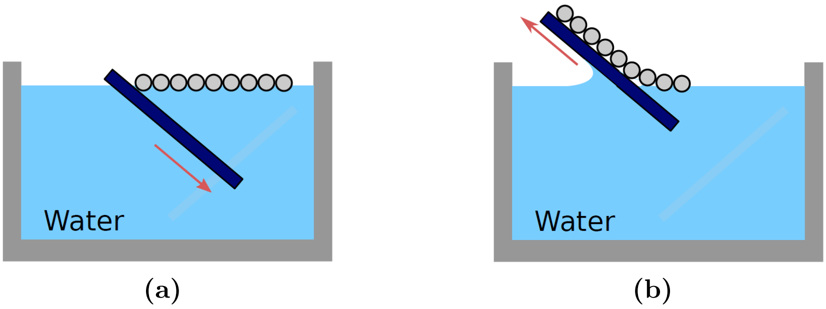

Figure 3.5: Procedure to pick up PS monolayer formed on the water surface. First the substrate is dipped in water **(a)**, then it is carefully extracted bringing the mask with it **(b)**.

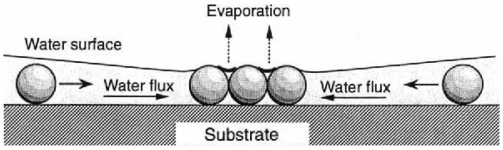

Figure 3.6: Schematic description of the nanospheres aggregation process.

evaporation.

The aggregation process in an ordered monolayer (figure 3.6) is due to the lateral capillary forces which are generated when the thickness of the solvent layer is lower than the spheres' size. This attractive force is composed of two principal factors: hydrostatic pressure and superficial tension due to the spatial variation of the liquid surface slope. This capillarity force pushes together the spheres, compacting them to form an ordered aggregate. Once an ordered nucleus is assembled, the evaporation process generates a convective flux of surrounding liquid that tends to compensate the evaporation and carries towards the ordered nanospheres. The free particles are attracted and attacked by capillarity forces to the ordered nucleus which grows gradually to form the mask, when the complete evaporation of the solvent occurs [62].

In the figure 3.7 (a, b) we can see some examples of the synthesized masks. It is worth noting the wide dimensions and distinctive iridescent color of the mask, due to the two-dimensional lattice of PS nanospheres. The masks produced are then charac-

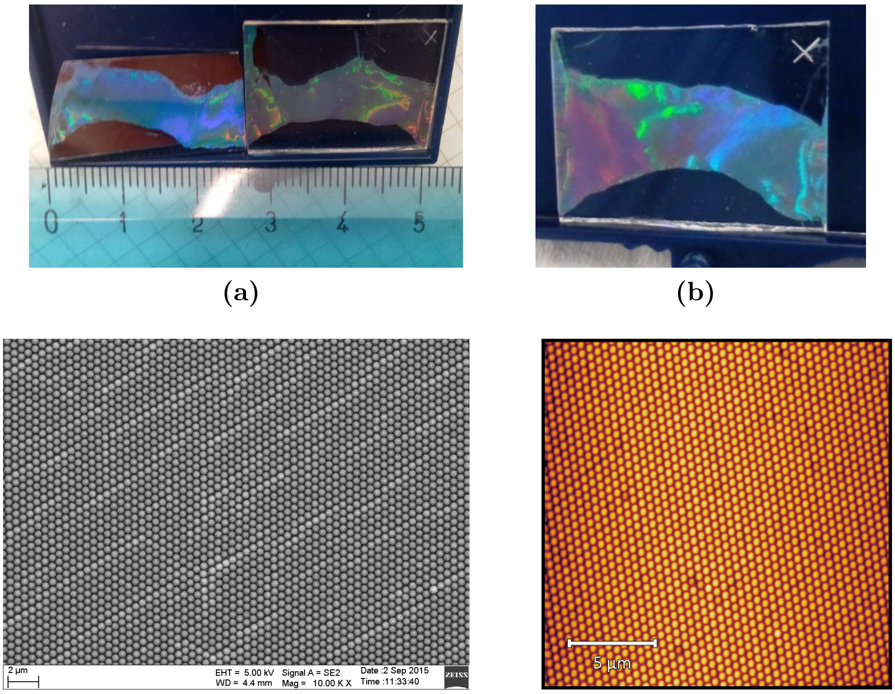

(a) **(b)**

(c) **(d)**

Figure 3.7: Mask made of 522 nm diameter polystyrene nanospheres. In the two photos, it is worth noting the wide dimensions (**(a)**, **(b)**) and the iridescent color. **(c)** and **(d)** show SEM and AFM images of a mask, respectively.

terized with different techniques. As an example in figure 3.7 (c, d) it is reported an example of morphological characterizations made by SEM and AFM measurements. From these measurements we can directly control the quality of the mask seeing and estimating the amount of defects such as vacations, dislocations, grain boundaries or poly-domains. However, these techniques explore a relatively small area (μm^2) compared to the size of the sample (cm^2). Optical characterization techniques, such as optical diffraction or UV-VIS-NIR spectroscopy, will be described in the following sections. These techniques allow a more immediate estimate of the mask quality further having the ability to quickly explore large areas.

3.1.2 Optical Diffraction

The obtained mask is a two-dimensional hexagonal close-packed lattice of PS nanospheres; since we have used nanospheres with 522 nm diameter, their dimension is comparable with visible wavelengths, hence we can study the mask quality by optical diffraction.

The monolayer of nanospheres acts as a diffraction grating, where every single sphere diffuses the light according to Mie's description [25].

A He-Ne laser source (λ543.5 nm) was used for the measurements. The laser beam is placed at normal incidence on the sample and the angle at which emerges the first maximum can be estimated from

$$n_{eff}\,\frac{\sqrt{3}}{2}a_0\,\sin\theta = \lambda_0 \qquad \Rightarrow \qquad \theta \simeq 62^\circ \tag{3.2}$$

where $\lambda_0 = 543.5\,\text{nm}$ is the wavelength of incident beam in free space, $\frac{\sqrt{3}}{2}a_0$ is the grating period and n_{eff} is the effective refractive index in the nanosphere layer that can be calculated via

$$n_{eff} = n_{PS}\Phi_{PS} + n_{air}\Phi_{air} \simeq 1.36 \tag{3.3}$$

where $n_{PS} \simeq 1.59$ is the polystyrene refractive index, $n_{air} \simeq 1$ and $\Phi_{PS} = 0.605$ and $\Phi_{air} = 0.395$ are the volume fractions occupied by PS nanospheres and air, respectively.

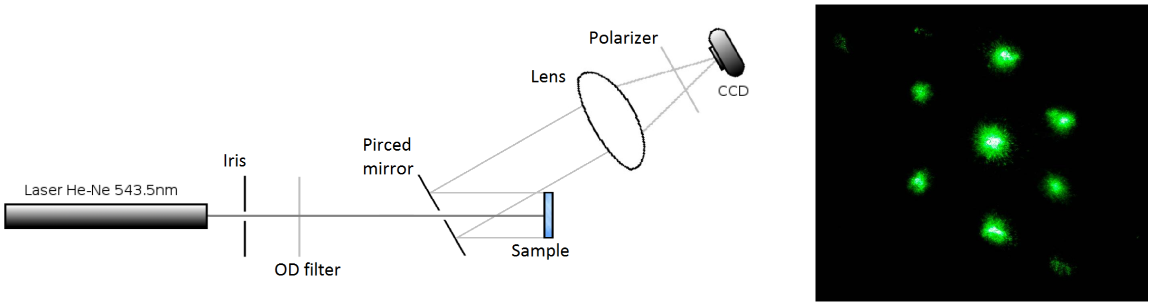

(a)

(b)

Figure 3.8: **(a)** Set-up for optical diffraction measurement. **(b)** diffraction pattern of a two-dimensional hexagonal close-packed lattice of 522 nm PS nanospheres.

However, the critical angle between substrate and air is about 41°, hence the diffraction pattern remain confined inside the substrate. For this reason, a pierced mirror is placed as shown in figure 3.8a, in order to project the image on a CCD camera with the aid of a lens to focus the pattern.

In Figure 3.8a it is possible to see the scheme of the optical diffraction set-up composed of a He-Ne laser, an iris that defines the beam dimension ($\sim 1\,\mathrm{mm}^2$), the pierced mirror which is rotated at about 30°, the sample, the lens and the CCD camera.

In Figure 3.8b, an example of the acquired diffraction pattern is reported and it gives us information about the scanned region. In fact, from the figure one can deduces the level of order of the mask. A hypothetical infinite perfect lattice produces a diffraction pattern with narrow spots. The presence of point or line defects spread the light spots. Furthermore, the presence of polydomains can lead at different effects on the diffraction pattern. If the poly-domains do not have a random direction but are within a narrow angular range around a preferred direction, the light spots are spread and it is possible to see thin lines called texture. Otherwise, with a completely random polydomains, rings appear in the diffraction pattern. These rings are called Debye-Scherrer rings. Then, a diffraction pattern as shown in Figure 3.8b identifies a good arrangement of the PS nanopheres.

In addition, we can identify the high symmetry axes of the lattice. From Figure 3.8b, the line joining two opposite points identifies a high-symmetry direction of the system along ΓK direction of the reciprocal lattice.

3.1.3 UV-VIS-NIR spectroscopy

Since the mask is a photonic crystal with a band structure that determines the interaction with the incident radiation, the mask quality can be evaluated via absorbance spectra by analysing the shape of the peak on the spectrum: the higher and narrower is the peak, the better is the mask correspounding [63].

For these measurements, a Jasco V-670 and an Ocean Optics spectrometer have been used. The principal difference of these instruments is the spectral working range: the Jasco V-670 works from 190 to 2600 nm while the Ocean Optics works from 100 to

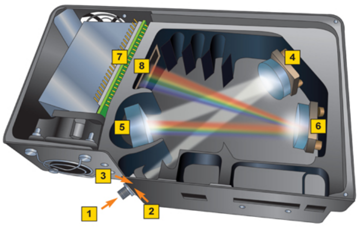

Figure 3.9: Schematic description of Ocean Optics detector HR-4000: 1) Optical fiber connector. 2) Slit. 3) Filter. 4) Collimating mirror. 5) Grating. 6) Focusing mirror. 7) CCD detector. 8) Collection lens.

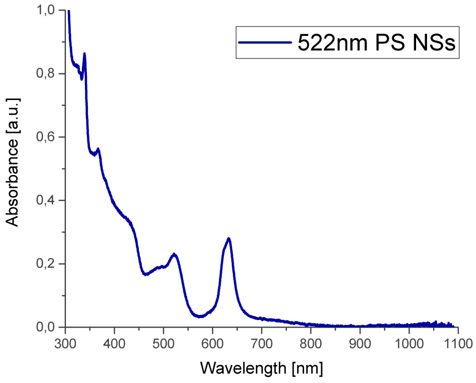

Figure 3.10: Absorbance spectrum of a PS mask with 522 nm diameter spheres.

1200 nm.

In particular, Jasco V-670 has two lamps to cover the entire operating range, a deuterium lamp ($190 - 350$ nm) and a halogen lamp ($330 - 2700$ nm). The working wavelength is selected by two gratings and the selected beam is driven on the sample perpendicularly to the surface. The signal in transmission is captured by UV-VIS detector (for the UV and visible range) and PbS photoconductive detector (for the near-infrared region).

The Ocean Optics spectrometer is composed of two elements: the source (DH-2000 BAL) and the detector (HR4000). The source DH-2000 BAL has a deuterium and a halogen lamp which cover a wavelength range from 215 to 2500 nm. The emitted light passes through a series of mirrors and filters to homogenize the intensity of the whole range and after that it is transmitted to an optical fiber with a diameter of 600 μm that collimates the beam on the sample, with a lens placed at its end.
The detector HR-4000 collects the beam by the optical fiber, as shown in figure 3.9: a mirror collimates the radiation on the grating that diffracts and directs the light onto the focusing mirror and then in the CCD detector. Each pixel on the CCD detector responds to the wavelength of light that strikes it, creating a digital response.

In Figure 3.10 it is shown as an example an absorbance spectrum of a mask recorded with the Ocean Optics spectrometer. From this spectrum, it is possible to extract information about the quality of the synthesized mask. For the used PS nanospheres with diameter of 522 nm, an absorbance peak arise at the wavelength of 640 nm, as we can see in Figure 3.10. The spectral position of the peak can be associated to the PS nanospheres' size. Whereas, the intensity and bandwidth of the absorbance peak can be associated to the quality of the photonic crystal. The higher and narrower is the peak, the fewer defects are present in the photonic crystal, then the better the mask.

3.2 Reactive Ion Etching

To synthesize the nanostructures chosen for this project i.e., the *nanodome array*, an etching process is used in order to reduce the nanospheres' diameter and preserve the ordered arrangement. This introduces a degree of freedom to modify the resonance wavelength of LSP because the spectral position depend on the nanostructures' size, as described in Chapter 1. In this way we can tune the plasmon resonance frequency at the peak of the fluorescent selected dye.

To do this the *Reactive Ion Etching* (RIE) technique was used [64]. The RIE consists in a dry ion-assisted chemical etching process which uses a chemical reactive plasma to erode several materials. Depending on the material to be etched, we have to choose the right type of gas to adopt. In this work the PS NSs are etched by a gas mixture of oxygen (O_2) and argon (Ar). Oxygen reacts chemically with the PS mask while argon, given its inert nature, sputters some of the material by transferring kinetic energy, thus etching the sample physically.

Inside a vacuum chamber, with a pressure of about 10^{-3} mbar, the samples are placed on an electrically isolated plate. Inserted the gasses, the plasma is generated by a radio-frequency (RF) electromagnetic field (of 13.56 MHz). The plate is negatively charged hence positive ions are attracted and driven towards the samples. Since the

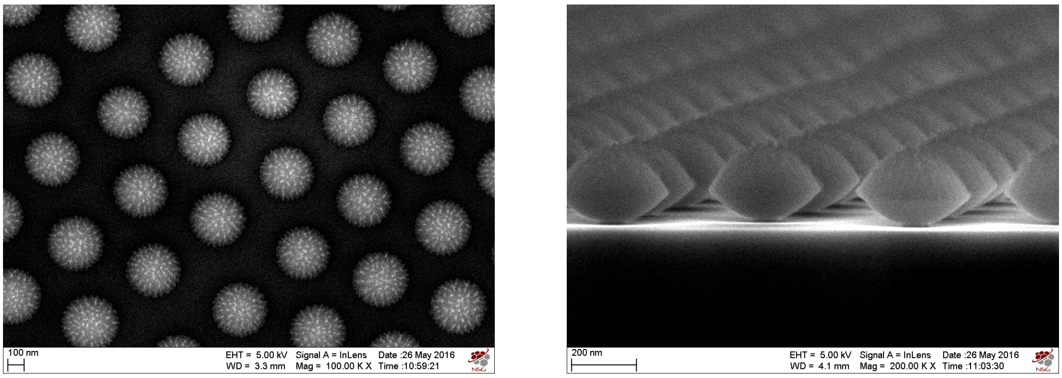

(a) Top view **(b)** Cross section

Figure 3.11: SEM images of a 522 nm PS nanosphere array after 7 min RIE. The final height of the nanospheres is of about 250 nm and the diameter of 335 nm.

ions collide on the masks perpendicularly, the process is particularly anisotropic and the spheres are etched especially in the vertical direction.

The etching process depends on several factors, such as the gas flux, RF power and chamber pressure which were previously calibrated. The etching time is the free variable used to get the desired spheres' size. In the present work, an etching time of 7 minutes was used in order to reduce the spheres diameter down to about 335 nm.

A SEM image of the resulting mask is reported in figure 3.11. It can be noted in **(a)** that the spheres are reduced in diameter, while the grating period is maintained. Two different regimes of etching are possible at low and high pressure, as shown in Figure 3.12. The low-pressure etching has less gas flow and ions can easily diffuse towards the sample driven vertically by the electric field. Therefore, an anisotropic erosion on vertical direction is performed. On the other side, a higher gas flow leads to a more isotropic etching of the spheres.

Another detail to note is the roughness of the spheres, very low in our case but adjustable by means of the ratio between the different gases.
Furthermore, we have to pay attention to the collapse of nanospheres caused by excessive erosion: this phenomenon imposes a maximum limit of the final spheres' diameter which is about half of the initial value.

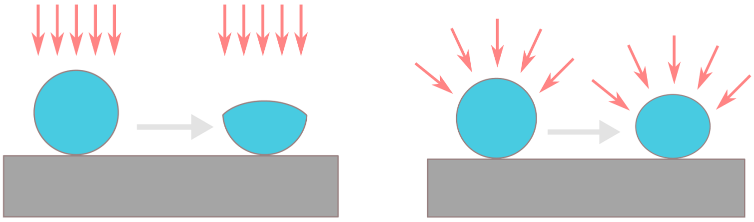

(a) Low pressure **(b)** High pressure

Figure 3.12: The two types of RIE etching.

3.3 Metallic Deposition

After the RIE process and the mask characterization, we proceeded to create the plasmonic nanostructures by metal deposition. However, to have a substrate that is more stable mechanically, thermally, physically and chemically, a silica layer is deposited upon the etched PS nanospheres and before the gold one. The sequential deposition of silica and metal is performed by *magnetron sputtering*.

3.3.1 Magnetron Sputtering

The deposition technique called *magnetron sputtering*, schematized in figure 3.13a, is a Physical Vapour Deposition (PVD) method by which atoms or molecules are ejected from a target material by high-energy particle bombardment so that the ejected atoms or molecules can condense on a substrate [65]. The energetic particles may be ions, neutral atoms, neutrons, electrons or photons, but the main sputtering applications are performed under bombardment with ions of a gaseous material accelerated by an electric field.
Usually gases are used as ion sources, because it's easier to ionize atoms when they are in a gaseous state. Noble gases are used to avoid the reaction of the gas with the target or the growing film. Typically utilized gases are Radon, Xenon, Krypton and Argon, but the most used for sputtering deposition is the last one, because it is easily available and cheaper.

The number of target atoms ejected per incident ion is called *sputtering yield* and depends on parameters related to the incident ion (energy and mass) and to the target (binding energy and mass). Furthermore, the deposition efficiency depends on the chamber pressure, because the gas presence generates collisions during the target atoms diffusion decreasing the number of atoms that reach the samples, as well as of the degree collimation. However, at low pressure, the sputtering efficiency decreases due to low number of ions that impact on the target. For these reasons, the working condition is

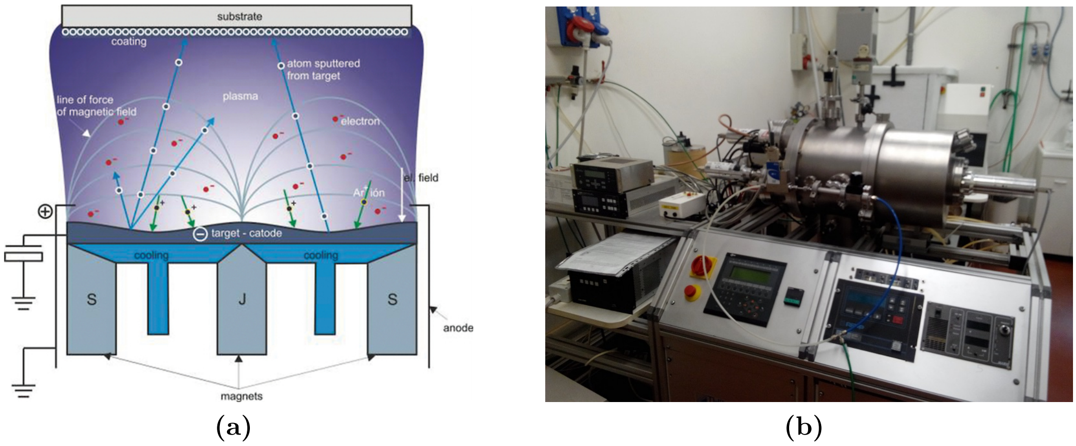

(a) (b)

Figure 3.13: Magnetron sputtering. **(a)** Schematic representation of the process. **(b)** Photo of the used machine.

set at a pressure of about 5×10^{-3} mbar.

The target is the material that one wishes to sputter, whereas the substrate is the material that one wishes to coat. The first is the cathode of an electrical circuit and has high negative voltage applied to it; the second is placed on the anode. These electrodes are placed inside a chamber, which is evacuated at pressure of about 10^{-6} mbar and successively a gas (for our purpose it is Ar) is introduced to create a dynamic vacuum at pressure of about 5×10^{-3} mbar. The electric field accelerates electrons, which in turn collide with Ar atoms, generating Ar ions (Ar^{+}) and more electrons. The gas becomes totally or partially ionized and so a plasma is created. Electrons are accelerated to the anode, while Ar^{+} ions are accelerated to the cathode and, when they strike the target cause the sputtering of atoms, which will be deposited on the substrate.

Often, the target erosion by plasma ions needs very long times, because plasma is weakly ionized and the ion current density on the target is low. For this reason, the *magnetron effect* is used: a magnetic field is superimposed to the electrical one to confine the electrons in a region near the target, avoiding their migration to areas far from the plasma and increasing in this way the plasma density. This effect is created by a series of magnets mounted below the target that generate field lines over the target, parallel to its surface
As a consequence, there is a reduction in the loss of electrons outside the plasma and an increase of the ionizing collision frequency, determining an enhancement of the ionization degree in the cathodic region and so an enhancement of the sputtering yield and the deposition rate.

Concerning the silica target, in a DC diode sputtering system as the one described, the sputtering glow discharge cannot be sustained, because of the immediate build up of a charge of positive ions on the front side of the insulator. Therefore, to sustain the glow discharge with an insulator target, the DC voltage power supply is replaced by a Radio-Frequency (RF) power supply, that avoids the accumulation of the ions.

The sputtering machine used in the present work is shown in figure 3.13b. It consists of a vacuum chamber inside which there are three torches which act as cathode: two are RF sources and one is a DC. In front of the targets, it is placed the sample holder that acts as the anode. Rotary and turbomolecular pumps create the first high vacuum

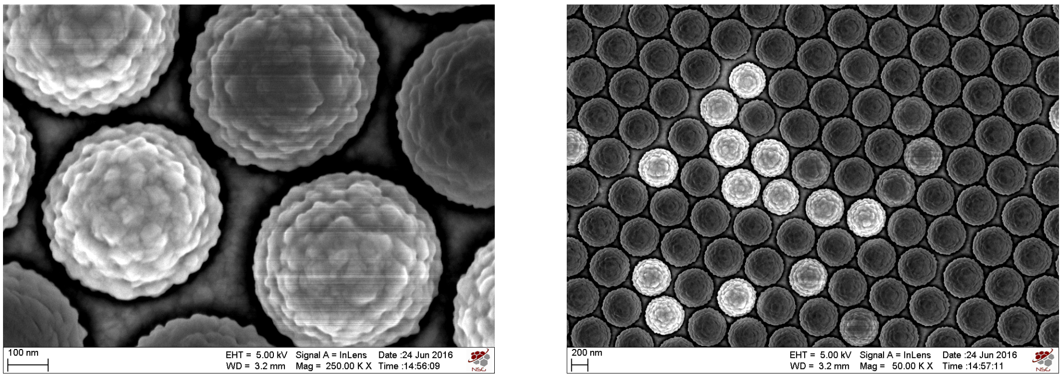

(a) **(b)**

Figure 3.14: SEM image of a gold nanodome array at different magnification (top view).

and subsequently maintain the dynamic vacuum made by the argon gas whose flow is electronically regulated by a fluximeter.

The sample holder distance can be varied, and also can be set in rotation for a more uniform deposition. In the present work it was placed in the farthest position from the torches in order to avoid an excessive thermal radiation that can damage the PS nanospheres.

Figure 3.14 shows two SEM images (in plan view) at different magnification of a gold nanodome array, after the magnetron sputtering depositions.

3.3.2 Thermal Evaporation

For the synthesis of triangular nanoprism arrays, the deposition process needs a higher degree of collimation in order to avoid the closure of the interstices between the spheres that, in this case, are not reduced in diameter by the etching process.

Therefore, to fabricate these nanostructures, the metal is thermally evaporated upon the mask, which later is removed by lift-off, leaving on the substrate the honeycomb structure of triangular nanoprisms, as shown in figure 3.15 with a SEM image.

The evaporation process takes place in a vacuum chamber at a pressure below 3×10^{-5} mbar to limit the presence of impurities and have a good level of collimation. The samples are placed above a tantalum (Ta) crucible containing the metal to evaporate. Then, the crucible is heated by Joule effect with a high current, up to the temperature necessary to obtain metal evaporation.

The current controls the temperature and consequently the deposition rate which is monitored by a *quartz crystal microbalance* placed close to the samples. This microbalance measures the electrical resonance frequency variation of a quartz oscillator due to the deposition of material on its surface. In addiction, a device connected with the microbalance calculates the deposition rate and the total thickness of the evaporated metal by setting different parameters such as the king of metal and the difference in height from the samples.

Furthermore, a shutter is placed between the samples and the crucible in order to

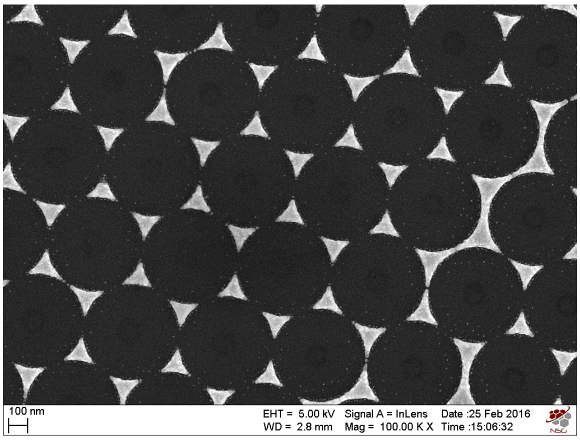

Figure 3.15: SEM image of a triangular nanoprism array, fabricated by nanosphere lithography from 522 nm PS nanospheres.

prevent the uncontrolled transient during the metal evaporation ignition and then to guarantee a more uniform deposition rate.

3.4 Dye-Doped Layer Preparation and Deposition

Once characterized the synthesized nanostructures, we proceeded to the deposition of the dye-doped film upon the samples.

Since our deal is to fabricate a device that works in the near-infrared region we needed a gain medium that emits in the region around $700 - 1000$ nm. For our purpose then we have chosen the laser dye *Styryl 9M* made by *Lambda Physik*; its factory features are listed in appendix A. We have chosen this dye also for its easy processability in a polymer matrix.

The dye is conserved in form of little solid crystals and it is dissolved in Acetone at the concentration of 4×10^{-4} M. Poly (methyl methacrylate) (PMMA) produced in pellets by *CRP* (*Centro Ricerche Plast-OPTICA*), is dissolved in acetone as well at 10% in weight.

The two solutions are mixed in proportion 1:3 in order to create a solution of Styryl 9M molecules and PMMA monomers dissolved in acetone with a dye concentration of about 10^{-4} M.

The nanostructured sample is placed on the bottom of a little pool with a volumetric capacity of 3 ml (Fig. 3.16). Hence, 2 ml of the liquid solution are poured into the pool with a microlitre pipette and left to dry for about 12 hours at room temperature. Room temperature evaporation of the solvent was chosen to avoid high temperature or UV exposure which could damage the nanostructures or the dye molecules.

With this technique, we are then able to create homogeneous dye-doped films with a thickness of about 100 μm, in contact to the plasmonic nanostructures. The thickness of the dye-doped film can be varied, by changing the volume of solution inside the pool.

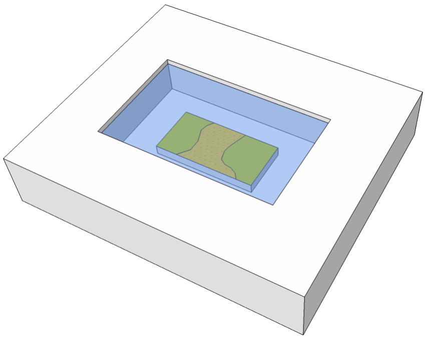

Figure 3.16: Depiction of the deposition pool used to form the dye-doped polymer film.

Chapter 4

Characterisation of Samples

The characterization of the synthesized samples is focused on their morphological and linear optical properties. The morphological ones are analysed by *Scanning Electron Microscopy* (SEM) and *Atomic Force Microscopy* (AFM). On the other hand the optical characteristics, extremely important for the purposes of the present work, are widely investigated by different techniques.

The linear optical response of our nanostructured samples is characterised by reflection measurements at normal incidence and collection. In addition, measurements as a function of the angle have been made in order to extrapolate information about the band structure of photonic crystal.

Furthermore, absorption and emission spectra of the chosen dye are performed by transmission and fluorescence measurements.

Finally, *photoluminescence* (PL) spectroscopy is used to verify and analyse the lasing emission properties of the synthesized devices.

4.1 Scanning Electron Microscopy (SEM)

A precise morphological characterisation is made by *Scanning Electron Microscopy* (SEM). This microscope allows to overcome the diffraction limit, succeeding to have nanometer resolution thanks to the use of electrons. Referring to figure 4.1a, we are going to describe now the operation principle of a SEM microscope. An electron gun generates electrons by the thermionic effect and consequently the free charges pass through a series of condenser lenses and apertures which select and focus the electron beam. After that, deflectors direct the beam on the sample and a last lens is placed to correct the beam shape which has to be circular in order to avoid astigmatism effects on the extrapolated image.

The instrumentation and the samples are placed inside a vacuum chamber and kept at a low pressure of about 10^{-6} mbar, because the electron gun must work at high temperature, and thus the electromagnetic lenses need a clean environment and to prevent that the presence of gas disturbs the electron path.

When the electron beam collides on the sample, the electrons can be subjected to different scattering effects. If the electrons collide with those of the external orbitals of the surface atoms, then inelastic scattering occurs and the beam loses much of its

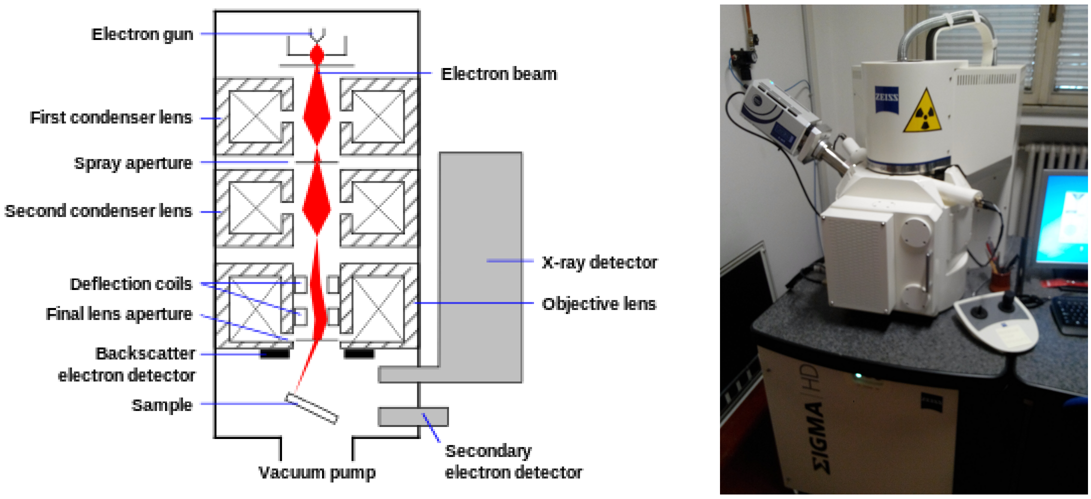

(a) Scheme. **(b)** Photo.

Figure 4.1: **(a)** Schematic description of SEM operation. **(b)** Photo of the used SEM Zeiss.

kinetic energy. The electrons that undergo this effect are called secondary electrons and they are collected by an in-lens detector.
On the other hand if the electrons collide with those of the innermost orbital or directly with the nucleus of the atoms on the sample surface, they undergo an elastic scattering and are backscattered and collected by a BSE (*backscattering electron*) detector. In addition to carrying information on the surface morphology, these electrons are influenced by the atomic weight of atoms hit, giving also information about the chemical composition of the material.
A further element of the chemical structure analysis are the X-rays generated by the rearrangement of the atomic electrons after the collision with the electron beam. These photons can be collected by an X-ray detector placed inside the vacuum chamber.

The resolution of the instrument is controlled by the degree of focusing and the kinetic energy of the electron beam. For the used microscope, Zeiss Gemini (shown in figure 4.1b), the resolution can range from 2.5 to 0.8 nm with potential differences between anode and cathode (electron gun) of 200 V and 30 kV, respectively.

Some SEM images at different magnification of the synthesized samples are shown in figure 4.2. These measurements were made with the in-lens detector due to its high signal to noise ratio and high brightness, which allows to obtain quickly a high resolution image, avoiding the beam to be incident for too long time on the sample, causing its alteration. In this work SEM has been used to obtain information with a high degree of details on the morphology of the synthesized nanostructures. From these images we can see very well the roughness of the surface and the detailed nanostructure shape. It is also possible to highlight if the nanostructures are in contact with each other or not. The SEM images were also elaborated with the ImageJ software which allows to assess the size of the nanostructures, for example, doing a statistical analysis on the diameter of a large number of nanostructures.

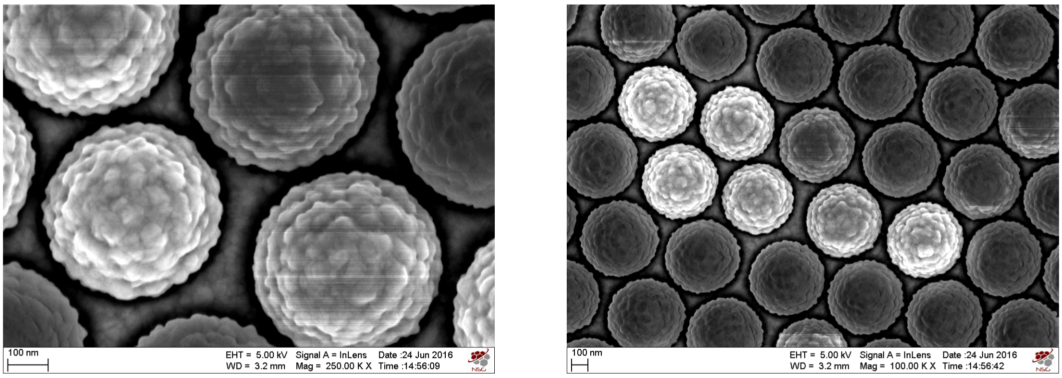

(a) 200 K **(b)** 100 K

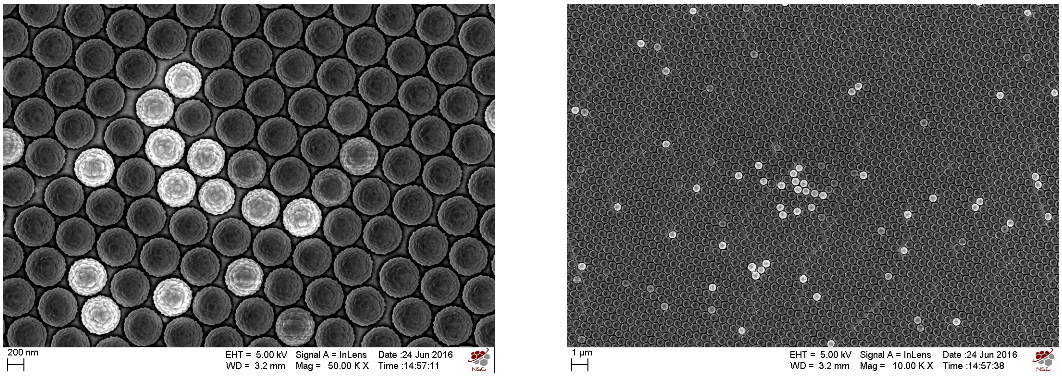

(c) 50 K **(d)** 10 K

Figure 4.2: SEM images at different magnification of a nanodome array (top view).

4.2 Atomic Force Microscopy (AFM)

The atomic force microscopy (AFM) technique is another very useful method to get morphological information of the samples. This technique of analysis was developed by Gerd Binning and coworkers in 1986 [66]. The main element of this instrument is a tip whose end has the size of about 10 nm, as shown in Figure 4.3a.

A scanning method is called *contact* mode. It is assumed an interaction between tip and sample described by a generic parameter P that depends strongly and uniquely by their relative distance z. By setting a value P_0 for this parameter, each height variation on the surface of the sample alters P. A feedback system can be used to maintain a constant tip-sample distance. The differential signal ($\Delta P = P - P_0$) is amplified and sent to a piezoelectric transducer which controls the tip-sample distance. The transducer uses the ΔP signal to change the distance and restore the sample towards the initial value, corresponding to $\Delta P = 0$. In this way it is possible control the tip-sample distance with high accuracy. When the tip moves in a given position (x;y) on the surface under examination, the signal $V(x, y)$ provided to the transducer is proportional to the distance from the ideal plane of the surface place at $z = 0$. This makes it possible to use the $V(x, y)$ values to map the surface topography, and get an AFM image.

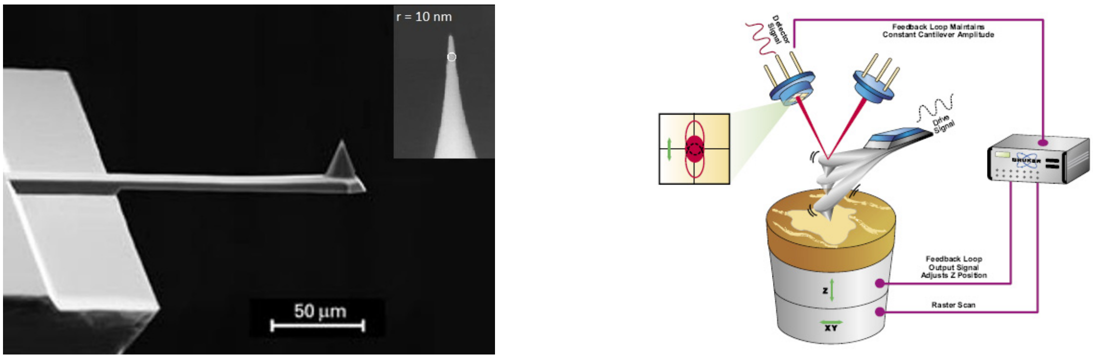

(a) (b)

Figure 4.3: (a) SEM image of an AFM cantilever, inset: SEM image of the AFM tip whose radius was measured. **(b)** Schematic representation of semi-contact measurements.

Another scanning method widely used is called *semi-contact* mode. In this case the tip with its support (a cantilever) are made to oscillate at their resonance frequency, with oscillations ranging from 10 to 100 nm in amplitude. The interaction between the sample and the tip, explicable by Van der Waals forces, causes variations of the oscillation amplitude and deformations of the resonance curve shape. Such variations are measured by the beam-bounce technique: the beam of a laser diode is focused onto the upper part of the free end of the cantilever, and is reflected and collected by a photodiode array which measures the changes in position and intensity of the reflected laser beam. Therefore by the measurements of the forces applied to the tip it is possible to obtain the sample morphology.

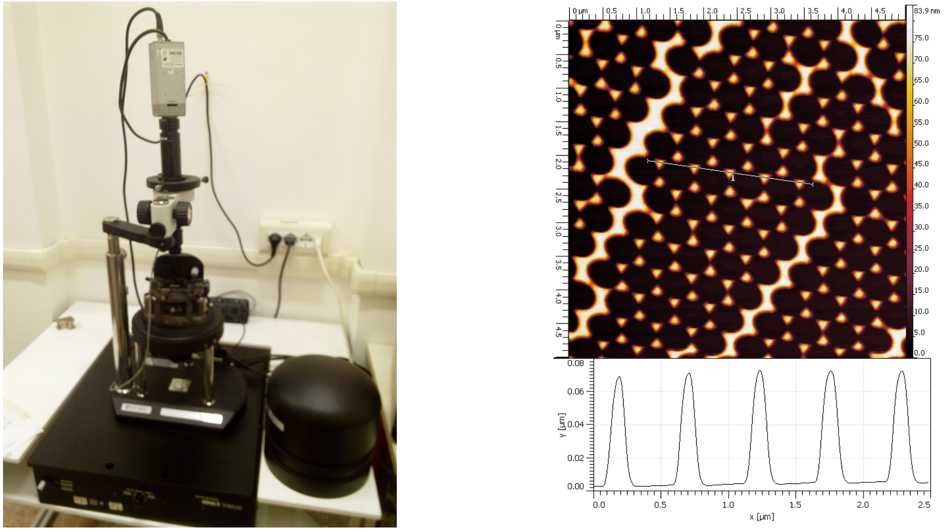

(a) (b)

Figure 4.4: (a) Photo of the AFM used in the present work. **(b)** AFM image of a triangular nanoprism array. Below, a 1D profile of the sample calculated by the software Gwyddion on the line visible in the AFM image above.

By a software (Gwyddion [67]) it is possible to display and analyse the collected data, measuring for examples the relative heights of structural elements or film thickness. In Figure 4.4b one can see an image made by AFM and the 1D profile of the sample and the line on which it was calculated. The distance between a peak and adjacent valley represents the height of the nanoprism on the substrate.

4.3 UV-VIS Spectroscopy

The linear optical properties of the nanostructured samples are obtained by measurements in reflection given that the gold film deposited is optically thick and does not allow transmittance measurements.

The measurements were performed not only at normal incidence and collection but also in an angle-dependent system. The first kind of measurements are performed with the set-up schematized in Figure 4.5a. The lamp and detector OceanOptics have been described in section 3.1.3. In this way it is possible to measure the reflection spectrum of the nanostructured samples synthesized in the present work. Then, this allows us to evaluate the extinction spectrum as $1 - R$, where R is the sample reflectivity. An example of the extinction spectrum in shown in Figure 4.6. By analyzing the extinction spectrum we can verify the presence of peaks that we can associate to plasmonic modes. This is used to optically characterize the metamaterials and to verify the coupling with the gain medium emission.

On the other hand, the angle-dependent measurements give us information about the band structure of photonic crystal formed by our nanostructures, discussed in the section 1.4.1. The component of the incident beam that couples with the nanostructure array is the one parallel to the lattice plane, labelled with $K_{//}$. By varying the incident angle, the component of wave vector coupled changes. Therefore, the intensity as a function of the wavelength of the reflected ray gives us information about interaction between radiation and the photonic crystal. From these data it is thus possible to reconstruct the dispersion law in a graph composed by energy E vs $K_{//}$, an example is shown in Figure 4.7.

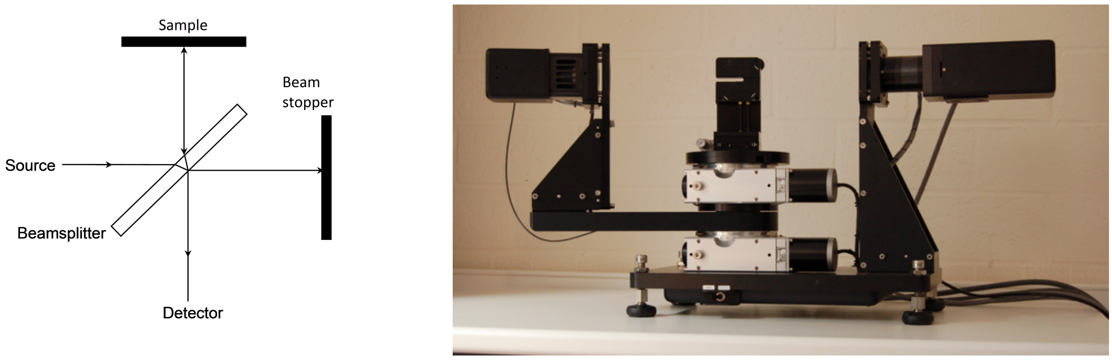

(a) (b)

Figure 4.5: **(a)** Scheme of the reflection measurements made with normal incidence and collection **(b)** Photo of the used instrumentation for the angular dependence measurements.

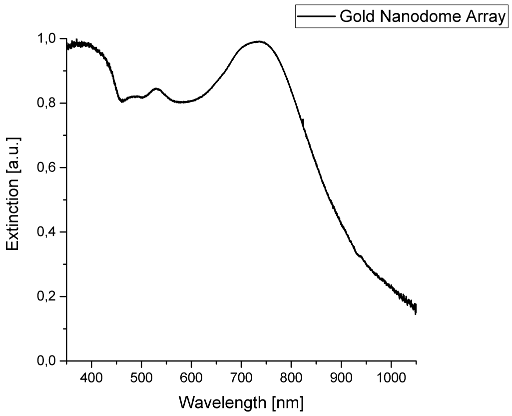

Figure 4.6: Extinction spectrum of a nanodome array (in air) calculated as $1 - R$ from reflection data.

The measurements are made thanks to mechanization of the angular movements of the two input and output arms, ensuring a high angular accuracy (see Fig. 4.5b). A xenon lamp (Xe) emits light which passes through a monochromator selecting the wavelength. Subsequently by an optical fiber, the light beam is driven to the fixed arm where it is polarized and collimated on the sample. The sample is vertically supported on a movable sample holder which determines the angle of incidence. A detector mounted on the output movable arm follows and collects the reflected beam acquiring the intensity data.

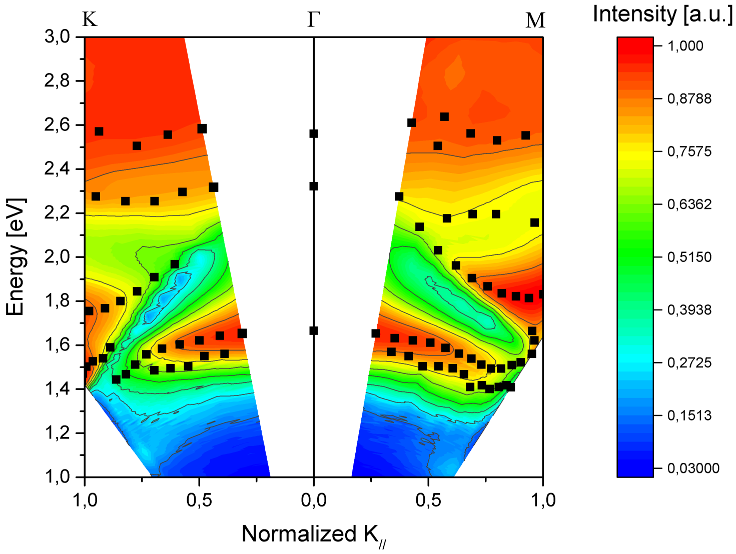

Figure 4.7: Dispersion law of the photonic crystal formed by the periodic arrangement of the gold nanodomes. The map is reconstructed from extinction spectra measured at different angles. $\mathbf{K}_{//}$ is normalized to the largest vector in first Brillouin zone along a given direction of high symmetry. The black points represent the extinction maximum.

In this case too, the extinction spectrum is calculated as $1 - R$, where R is sample reflectivity. In addiction the energy and the parallel wave vector are calculated via

$$E = \frac{hc}{\lambda} \tag{4.1a}$$

$$K_{//} = \frac{2\pi}{\lambda} \sin\theta \tag{4.1b}$$

where h is the Plank constant, c is the light speed in the free space, λ is the wavelength and θ is the angle between the wave vector of incident beam and the normal to the lattice plane. The reconstructed map identifies the band structure of the photonic crystal, giving the possibility to evaluate the presence or not of the photonic bandgap, as well as the behaviour of the photons in the crystal.

4.4 Photoluminescence Spectroscopy

The photoluminescence (PL) spectroscopy investigates the emission of light from a material after the absorption of photons. This first characterization step, unlike that for the characterization of the laser emission, has been done without an angle-dependent collection. It is then optimized the pump system and data collection as the Figure 4.8 shown.

The second harmonic (at 532 nm) of a *Q-switched Nd:YAG* laser is used as pumping beam. Then, this beam is attenuated by the interchangeable optical density (OD) filters (made by Thorlabs) in order to modulate the intensity of the beam. After that, the laser beam is directed onto the sample by two highly reflective mirrors for this specific wavelength. The intensity loss after this two mirrors was estimated lower than

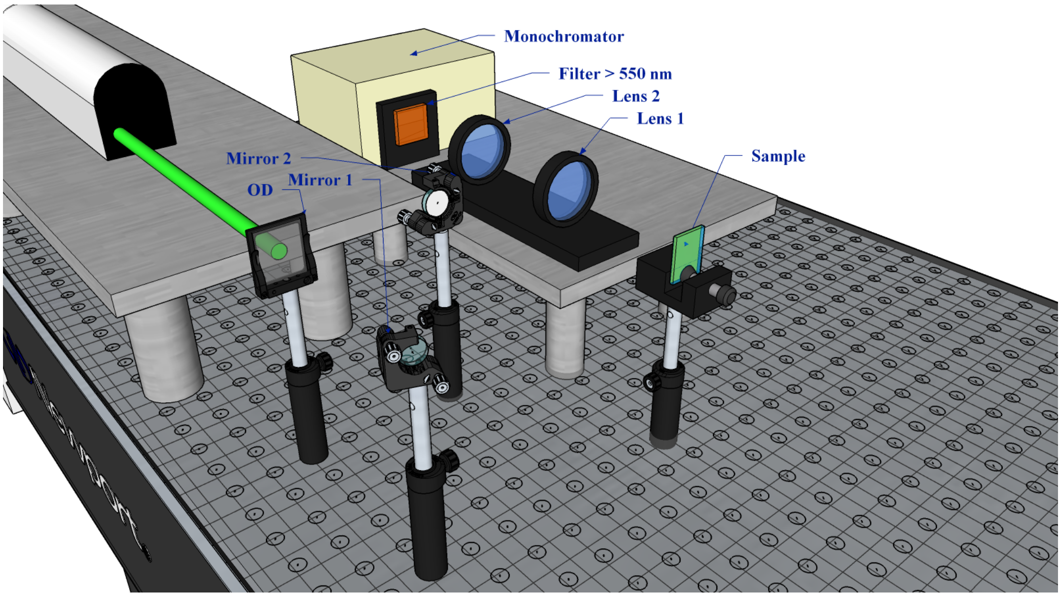

Figure 4.8: Schematic description of the optical set-up used for PL measurements. The incident angle of the pumping beam was fixed at 33°, while the collection is normal to the sample surface.

2 %.

The sample, placed with the surface normal to the direction of collection, is illuminated by the beam at an angle of about 33°. Two converging lenses (2” diameter) have been used to collect and bring the emitted radiation with an angular aperture on the sample of 30° (NA = 0.26). The collected radiation is focused on the entrance slit of a ORIEL single-grating monochromator, where a longpass filter ($\lambda > 550\,\text{nm}$) is placed. This provides the spectral discrimination of the luminescence signal, which is detected by a photomultiplier tube. For this characterization, we have used a HAMAMATSU N2-cooled R5509-72, operating in the $600 - 1400\,\text{nm}$ spectral range. The signal is then acquired with a digital oscilloscope (Tektronix TDS 7104) and the data have been stored by a home-made software.

On the other hand, regarding to the measurements for the nanolaser emission characterization, we have set-up an apparatus for angle-dependent collection measurements. The photo of the collection instrumentation is shown in Figure 4.10b, while the scheme of the optical set-up is shown in figure 4.9.

In this case the pumping beam passes through an iris with a diameter of 3 mm with a respective area of $7.1\,\text{mm}^2$. After that it is directed onto the sample by the two highly reflective mirrors.

The sample is placed on a holder which is positioned perfectly at the center of a rotating system but disconnected from this. On the rotating frame it is attached a guide which houses the collection set-up composed by a longpass filter $\lambda > 550\,\text{nm}$ and a 5× objective that focuses the collected radiation on the entrance lens of an optical fiber. The filter was placed to prevent that possible reflections of the laser may enter into the lens of collection and disturb the measurement. To maximize the collection efficiency, without significantly affecting the angular resolution, the objective has been

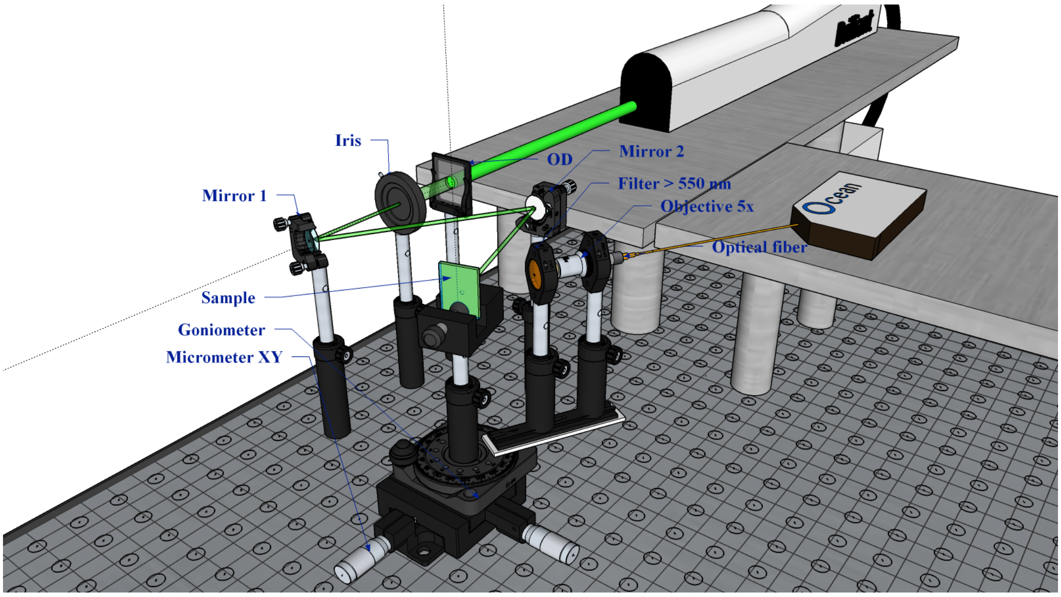

Figure 4.9: Schematic description of the optical set-up used for lasing emission characterization. The incident angle of pumping beam was fixed at 0°,i.e., perpendicular to the sample surface, instead the collection was made at different angles with respect to the sample normal.

placed at a distance of about 3.8 cm with an angular aperture which results of about 12° (NA = 0.1).
The fiber carries the signal to the detector OceanOptics HR-4000, discussed in the spectroscopy section 3.1.3. The data are transferred to a laptop and, with the software *SpectraSuite*, we can view and save the collected data.

The laser used in the present work (figure 4.10a) is a nanosecond pulsed Q-switched Nd:YAG laser (Blilliant by Quantel). It is a solid state laser where the active medium is a garnet of yttrium and aluminum ($Y_3Al_5O_{12}$) doped with neodymium (Nd). The medium is excited by stroboscopic lamps at a frequency of 10 Hz. By the technique of *Q-switching*, the laser emits pulses of 4.5 ns with a repetition rate (RR) that can be varied from 10, 5 or 2 Hz. In the present case the measurements were taken with a RR of 10 Hz.

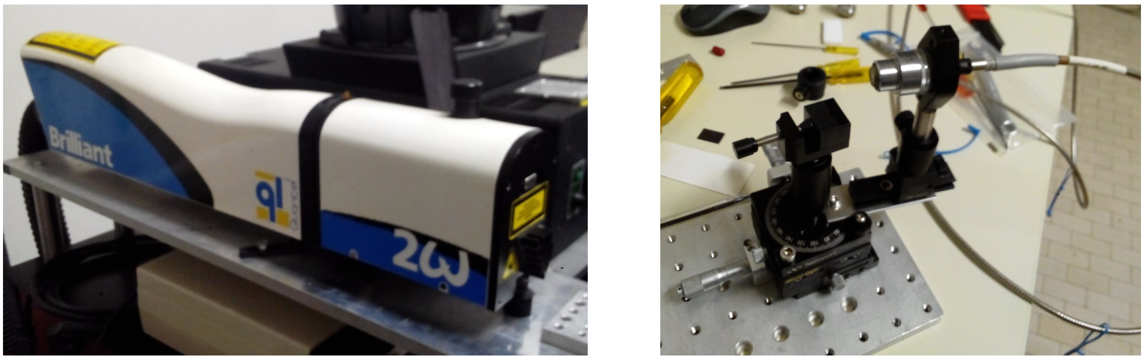

(a) Laser *Brilliant Q-switched* Nd:YAG.

(b) Sample holder and angle-dependent collection set-up.

Figure 4.10: **(a)** Photo of the used Nd:YAG laser. **(b)** Photo of the used angle-dependent collection set-up: a movable support is governed by two micrometers, above there is a goniometer to which a slide is fixed where a movable support holds the objective and the optical fiber; at the center of the goniometer but decoupled with this, it is placed the sample holder.

Chapter 5

Results and Discussion

In this chapter we will present the main results obtained in this thesis. First of all the most relevant results regarding the active medium and the nanostructured material will be discussed. Then we will go into the main topic of this work, i.e., the lasing action.

5.1 Dye-doped polymer films

The first analysis about the optical properties of the synthesized gain medium performed with the dye in liquid solution. The Styryl 9M is dissolved in ethanol at a concentration of about 10^{-4} M. The absorbance spectrum is acquired by UV-Vis spectroscopy (Section 3.1.3) with the OceanOptics spectrometer, while the emission spectrum is collected by our PL set-up (Section 4.4). Figure 5.1 shows the overlapping of the two spectra. The absorption peak is at a wavelength of 580 nm, while the emission peak at 810 nm. These values are consistent with those reported in the technical characteristics of the dye in the appendix A. We can note that this dye shows a large Stoke's shift, which prevents the self-absorption of the emitted photons, increasing the quantum efficiency and making it a good candidate for application as a gain medium in a laser system.

Since our goal is to implement the gain medium in solid-state form, the dye is

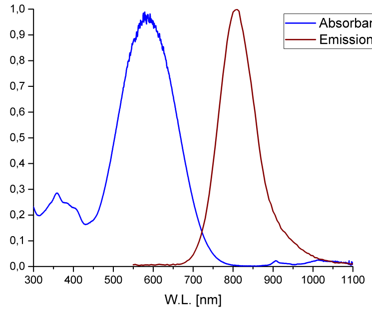

Figure 5.1: Absorbance and fluorescence spectra of Styryl 9M dissolved in ethanol.

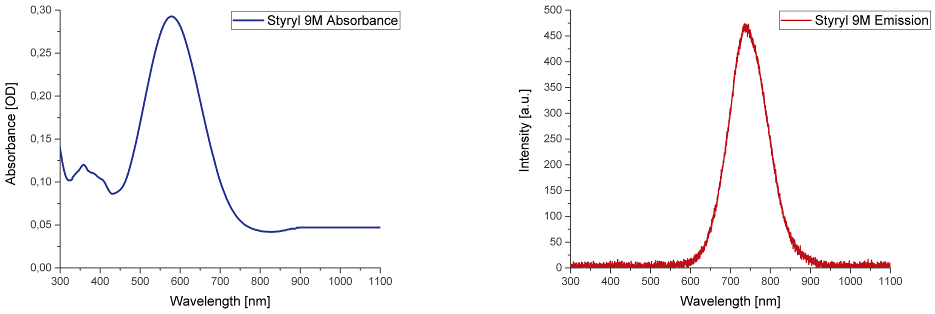

(a) Absorbance

(b) Emission

Figure 5.2: A PMMA film doped with Styryl 9M: **(a)** absorbance spectrum; **(b)** fluorescence spectrum.

embedded in a polymeric matrix, in particular PMMA. The dye-doped polymer film, formed by the procedure described in section 3.4, is then characterized. The spectrum of absorbance, shown in Figure 5.2a, shows a peak of absorption at a wavelength of 580 nm in line with that found for the dye in ethanol. On the left in Figure 5.2b the emission spectrum is shown, the fluorescence peak in this case is at a wavelength of 740 nm. The shift in the emission wavelength is of about 0.15 eV, this energy is consistent with that of vibrational states of the molecules, suggesting that some vibrational and rotational states may be inhibited by the polymeric matrix embedding the dye. Furthermore, we can also suppose that the matrix does not modify the electronic structure of the dye molecule since the absorption spectrum is not changed.

5.1.1 Bleaching

We have also verified the stability of the dye-doped film exposed to the laser beam investigating the characteristic of the bleaching process. This process, described in section 2.1.5, causes the loss of quantum efficiency of the system with the consequent lowering of fluorescence emission intensity. By PL measurements the fluorescence peak intensity is evaluated and reported as a function of the exposure time t.

We report the obtained results in Figure 5.3. In Figure 5.3a we see that at an energy density of about $1\,\mathrm{mJ/cm^2}$, the experimental points are fitted by a negative slop line, but the variation after a some hours is less than 10 %. Increasing the energy density, at $4\,\mathrm{mJ/cm^2}$ (Fig. 5.3b), the experimental peak intensity points follow an exponential decreasing with a characteristic time of 40 ± 3 minutes. Increasing drastically the energy density up to $20\,\mathrm{mJ/cm^2}$ (Fig. 5.3c) the experimental points are well fitted by a double exponential given by the formula

$$y = A_1 e^{-x/t_1} + A_2 e^{-x/t_2} + y_0 \tag{5.1}$$

where the free parameters t_1 and t_2 identify the characteristic times taken into account. In this case $t_1 = 1.9 \pm 0.2$ minutes and $t_2 = 16 \pm 2$ minutes. These times set a limit to the exposure time of the sample at a given energy density. However, we note that

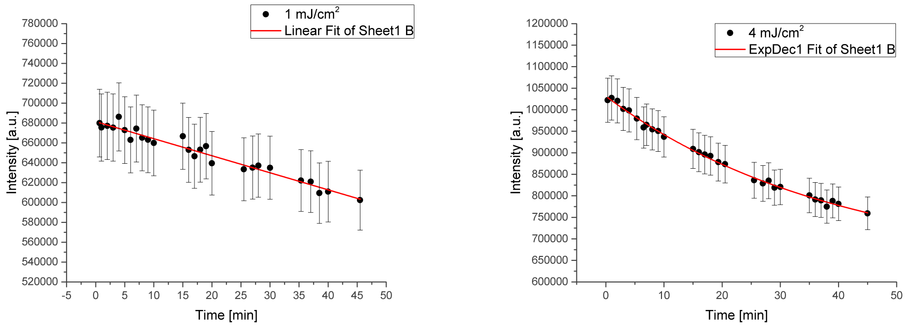

(a) $1\,\mathrm{mJ/cm^2}$

(b) $4\,\mathrm{mJ/cm^2}$

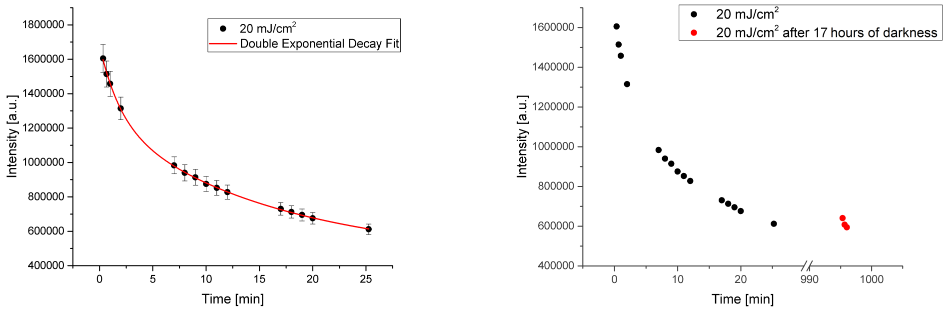

(c) $20\,\mathrm{mJ/cm^2}$

(d) $20\,\mathrm{mJ/cm^2}$ (black dots); $20\,\mathrm{mJ/cm^2}$ after 17 hours of darkness (red dots)

Figure 5.3: Photobleaching measurements at different energy densities of exposition: $1\,\mathrm{mJ/cm^2}$ in **(a)**, $4\,\mathrm{mJ/cm^2}$ in **(b)** and $20\,\mathrm{mJ/cm^2}$ in **(c)**. The black points represent the fluorescence peak intensity at the time t of exposition, while the red curve is the best fit of the experimental points. In **(d)**, the red points show the measurements of the fluorescence peak after exposure to the highest energy density and 17 hours of darkness.

such values of energy densities are quite high compared to typical working conditions that are around of $1\,\mathrm{mJ/cm^2}$. So bleaching is not expected to play a major role in our lasing system.

Furthermore, a possible recovery of the dye after the bleaching process has been verified. A recovery of the fluorescence is in fact seen in dye-doped polymer films by Howell and collaborators [68]. However, as it can be seen in Figure 5.3d after 17 hours of darkness no recovery occurs.

5.2 Plasmonic Nanodome Array

In the synthesis of the plasmonic nanolaser device, it is required that the plasmon resonance frequency of the nanostructured material overlaps the emission frequency of the dye. As explained in Chapter 1, the plasmon resonance frequency of the nanoarrays depends on several parameters: the shape, size, chemical composition and the surrounding dielectric. The polymer matrix chosen for the dye, PMMA, defines the

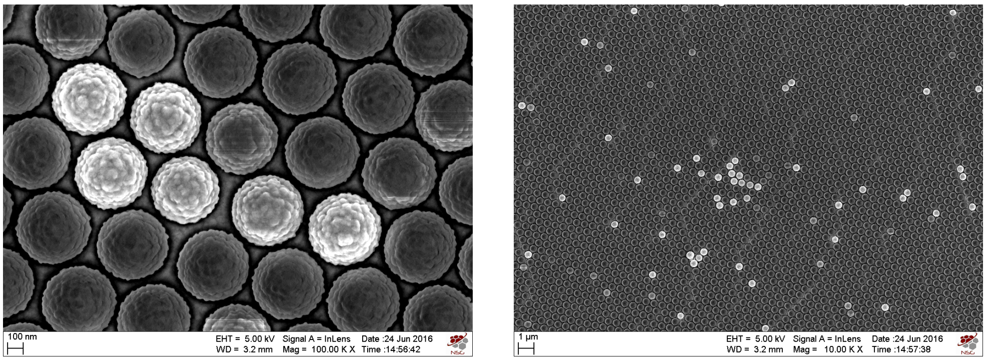

(a) (b)

Figure 5.4: SEM images of the gold nanodome array (top view).

dielectric environment of the nanparray embedding. The nanodome shape was chosen for its large scattering cross-section and gold is used for its compatibility and chemical stability. Then, the size of the nanostructure is the last parameter to work on in order to couple, as far as possible, the resonance.

During the synthesis process, described in Chapter 3, we can control the radius and the thickness of the gold nanodomes by varying the etching time and the deposition duration. Subsequently, SEM images (Fig. 5.4) of the nanostructured material are acquired and by the software imageJ, the diameter is estimated from the average of 25 domes for each sample. In addition, by profilometric measurements, the thickness of the silica and gold layers are measured.

Then as described in section 4.3, the reflection measurements are performed to evaluate the resonant peak of the plasmonic metamaterial. Reflection (R) data are

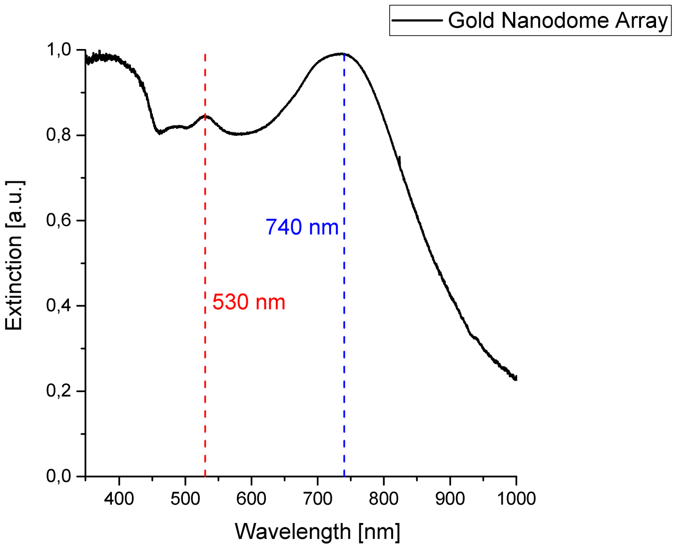

Figure 5.5: Extinction spectrum of a nanodome array (in air) calculated by $1 - R$ from reflection data.

converted into extinction graphs by plotting $1 - R$. Figure 5.5 shows the extinction spectrum of a nanodome array.
The spectrum exhibits two peaks: the most evident at a wavelength of 740 nm is associated with the LSP, in particular to the dipolar mode. This peak presents a large bandwidth (FWHM) of about 200 nm. The other at a wavelength of 530 nm can be associated to multipolar modes of the LSP. We can notice that the principal extinction peak appears where the maximum fluorescence occurs. But, the subsequent deposition of the polymer film shifts the peak at longer wavelength. However, from simulations the displacement still allows an overlap with the spectrum of the dye fluorescence. The purpose for the future consists in the improvement of this coupling which ensures better and more precise results.

This result was obtained starting from PS nanospheres with a diameter of 522 nm. The mask was then etched by RIE for 7 minutes with a flux of argon and oxygen in the ratio of 1 : 3 at a pressure of 9×10^{-3} mbar. This process has reduced the nanosphere diameter to 335±2 nm. Subsequently, by magnetron sputtering, 115±4 nm of silica and 78±2 nm of gold were deposited, thus obtaining an external diameter of the nanodomes of 465 ± 5 nm.

Ellipsometry measurements as a function of the angle of incidence, described in

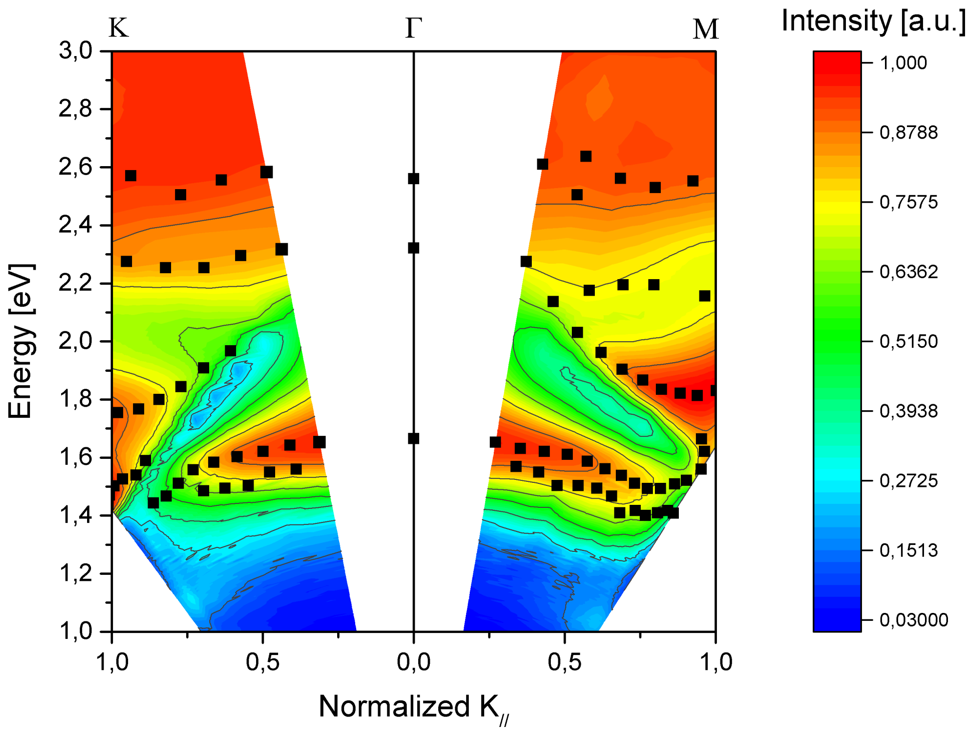

Figure 5.6: Dispersion law of the photonic crystal formed by the periodic arrangement of the gold nanodomes. The map is reconstructed from extinction spectra measured at different angles. $\mathbf{K}_{//}$ is normalized to the largest vector in first Brillouin zone along a given direction of high symmetry. The black points represent the extinction maximum.

section 4.3, enabled to reconstruct the map shown in Figure 5.6. The map represents the dispersion law $E(\mathbf{K}_{//})$ of the photonic crystal (section 1.4.1) formed by the periodic arrangement of the nanodomes. This map is reconstructed by the extinction spectra measured at various angles in two high-symmetry directions of the system along ΓK and ΓM direction of the reciprocal lattice. $\mathbf{K}_{//}$ (the component of the wavevector on the plane of the nanodome) and E are calculated using the equations (4.1) and $\mathbf{K}_{//}$ is normalized to the largest vector in first Brillouin zone along a given direction of high symmetry. The black points on the graph represent the extinction maxima of the spectra acquired at various angles.

Red areas represent high extinction of the incident beam due to the coupling radiation with the nanodome array. At high energy, the strong extinction arises due to the gold interband transitions, while the high extinction zone at about 1.5 eV is due to coupling with the LSP mode.
The blue areas, instead, are those where the reflection is greater, that is, the possible areas in which the photonic crystal inhibits the radiation propagation.

5.3 Lasing action

The final samples made by coupling the nanodome array to the gain medium according to the procedure described in Chapter 3, are finally characterized by PL measurements whose setup is explained in section 4.4. These measurements are carried out on three types of samples: (i) dye-doped films on a silica substrate; (ii) a dye-doped film on a gold thin film; (iii) dye-doped films over gold nanodome arrays. The dye-doped films in the various samples were made with the same procedure presented in section 3.4. To minimize possible differences in the dye-doped layer thickness and to avoid unwanted

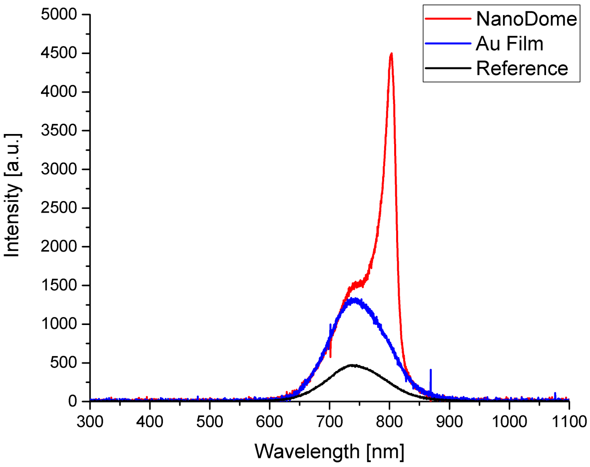

Figure 5.7: Comparison between three types of samples: dye-doped film on a silica substrate (Reference, black curve); dye-doped film on a gold thin film (Au film, blue curve); the final sample formed by the dye-doped film over a gold nanodome array (NanoDome, red curve). The measurements are taken at a collection angle of 25° and an energy density of 2.5 $\mathrm{mJ/cm^2}$.

parameters, it was decided to leave in the nanostructured samples an area adding the gold film (without the nanostructures) large enough to make PL measurements directly onto it.

The measurements are performed as a function of the pump energy density and collection angle. The results show that at a collection angle of 25° with respect to the sample's normal, where we detect an angular peak in the emission, and an energy density of 2.5 mJ/cm^2, the three samples are significantly different.

As you can see in the Figure 5.7, the nanostructured sample presents a narrow emission peak above the fluorescence curve, unlike the other types of samples. The peak occurs at a wavelength of 795 nm with a bandwidth (FWHM) of about 25 nm quite narrower compared to that of the fluorescence band of 100 nm. Following the literature, the sharp peak at 795 nm is interpreted as lasing emission. The lasing action can be inferred by the occurrence of a threshold effect in the pump energy, as we will describe in the next section. Nonetheless, it is important to note that the possibility of *amplified spontaneous emission* (ASE) has to be taken in to account as well. In order to definitely discriminate between lasing and ASE further measurements

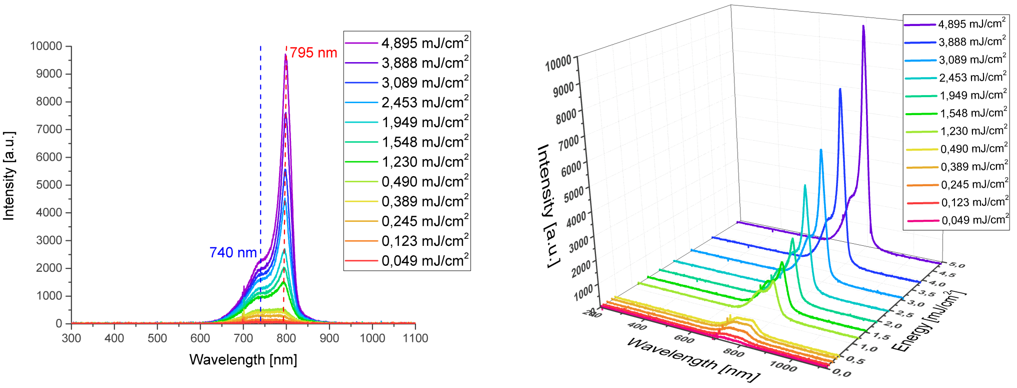

(a) Gold nanodome array **(b)** 3D plot of the data in **(a)**

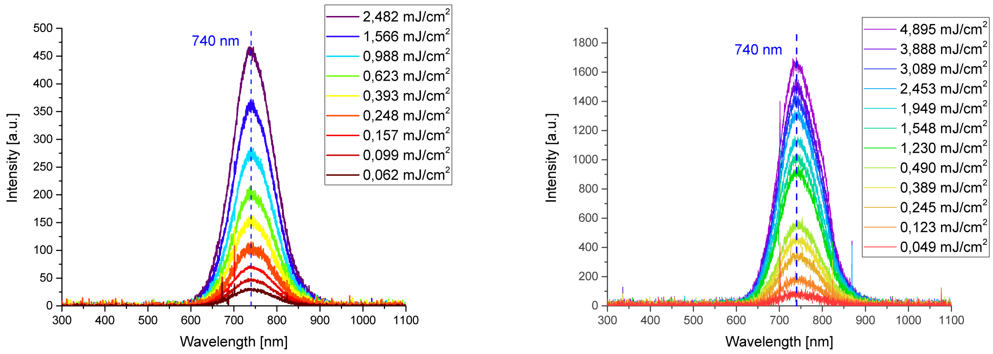

(c) Only dye-doped polymer film **(d)** Gold thin film

Figure 5.8: Comparison between the emission spectra as a function of energy density of the three samples: **(a)** the dye-doped film above a gold nanodome array; **(b)** the 3D plot of the data in **(a)**; **(c)** the dye-doped film; **(d)** and the dye-doped film above a gold thin film.

will be needed, which will be performed in the next future. Particularly, the temporal coherence of the emission will be investigated. In fact, the ASE emission presents no temporal coherence, and this also implies wider bandwidths than those of the laser emission.

We can also notice the difference between the fluorescence spectrum of the samples with and without the gold film (black and blue curves in Figure 5.7). The metal film reflects both the incident ray and the photons emitted by the dye molecules, with a reflectivity of 75 % and 97 % for the two wavelengths, respectively [69]. This could explain the increase in fluorescence signal with respect to the reference sample.

5.3.1 Lasing Threshold

By varying OD filters, it is possible to study the behaviour of the laser emission as a function of the pump energy density. We explored a range of energy density that goes from 0.05 mJ/cm^2 to 4.9 mJ/cm^2 for all the three types of samples at a collection angle of 25°. For the samples without nanostructures, fluorescence scales linearly with

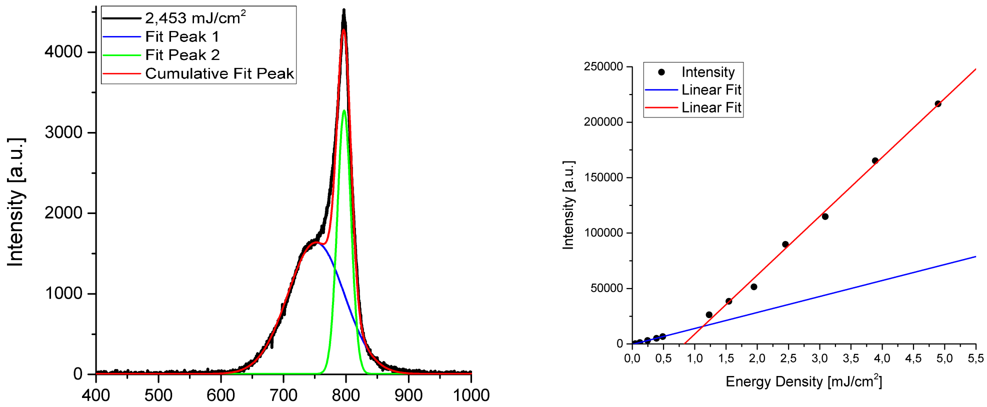

(a) Peaks analysis **(b)** Intensity

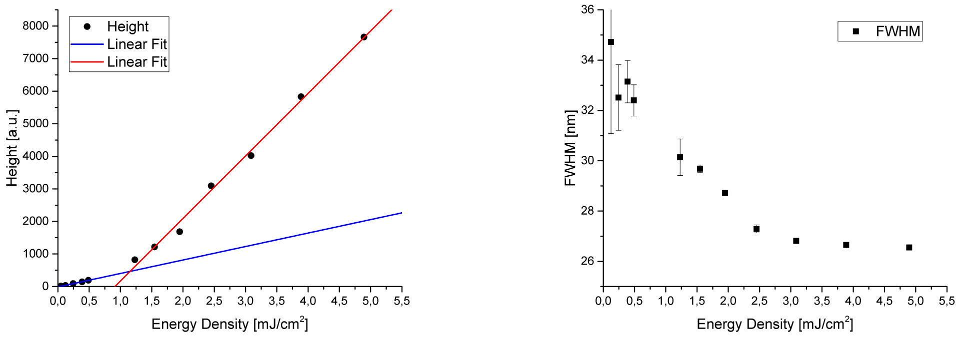

(c) Height **(d)** FWHM

Figure 5.9: **(a)** An example of the peaks analysis via a double-Gaussian fit. The laser peak parameters as a function of the energy density: **(b)** the integral subtended by the curve; **(c)** the height of the peak; and **(d)** the FWHM of the peak.

the energy density. Conversely, the sample with the gold nanodome array exhibits a different behaviour.

As shown in Figure 5.8, the laser peak arise for the sample with the nanodome array (**(a)**, **(b)**). By increasing the energy density, we can note that the laser peak drastically increases compared to the fluorescence one. In the same condition, the other samples without the nanostructures (**(c)** reference and **(d)** with the gold film) do not present any emission laser peak.

The laser peak parameters are estimated by deconvolution of the peaks via a double-Gaussian fit. An example of this analysis is shown in Figure 5.9a. The parameters taken into account are the integral subtended by the curve, the height of the peak and its FWHM. These parameters are plotted as a function of the energy density in Figure 5.9. We can note that the data, relating to the intensity and height (**(b)**, **(c)**), drastically increase after a threshold value changing the slope of the interpolation line. Around this threshold value in Figure 5.9d we can note a decrease of the FWHM. This threshold has been estimated by the intersection of the two fitted lines at a value of $1.2 \pm 0.1\,\mathrm{mJ/cm^2}$. We note that this value is well below the energy density where the photobleaching phenomenon becomes important (i.e., at about $4\,\mathrm{mJ/cm^2}$).

5.3.2 Directionality

The laser emission is strongly dependent on the collection angle. The directionality observed in the emission could be explained by considering the possibility of coherent scattering by nanostructures. Further investigations are in progress to clarify this consideration. To study the radiation pattern, angle-resolved measurements were performed with the set-up described in section 4.4. We explored a range between 15° and 80° with a step of 5°. The incident angle of the pump beam is fixed to 0°, perpendicular to the sample surface. The energy density was kept constant at a value of $2.5\,\mathrm{mJ/cm^2}$, above the threshold but below the limit of the photobleaching.

Figure 5.10 shows the emission map calculated from the angular measurements. The emission intensity is shown by the color scale and it is a function of the angle and the wavelength placed on the abscissa and ordinate, respectively. It can be noted the narrow emission peak at an angle of about 25° at the wavelength estimated before of 795 nm.

More measurements were made around the maximum laser signal, exploring a range between 16° and 34° with steps of 2°. The various spectra were analysed, deconvolving the laser peak from the fluorescence one having first removed adequately the base line and dark. The graph in Figure 5.11 shows the evolution of the laser peak intensity as a function of the collection angle. The data are fitted by a Gaussian curve with a centroid at 24° and a FWHM of 6°.

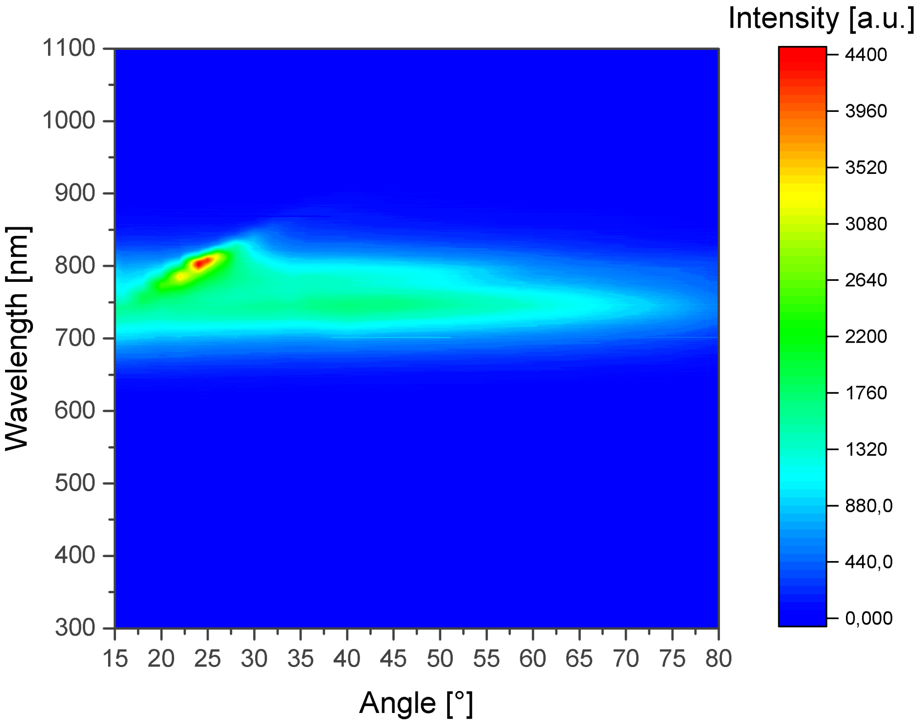

Figure 5.10: Map of the emission intensity as a function of the collection angle and the wavelength.

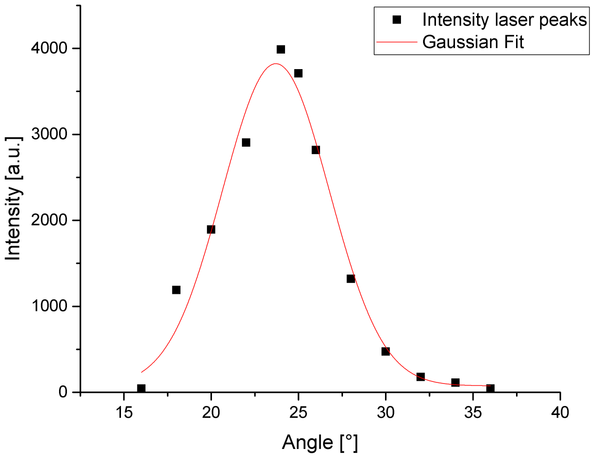

Figure 5.11: laser peak emission at different angles (black points) fitted by a Gaussian curve (red line).

Chapter 6

Conclusions

In this thesis it was presented the opportunity to obtain laser emission from a solid-state plasmonic nanolaser. The synthesized device emits laser light in the near-infrared region by the coupling between a gain medium and a plasmonic nanostructured material.

Gold nanodome arrays arranged in a two-dimensional hexagonal lattice have been designed, synthesized and characterised, with a period of 522 nm. The nanostructured metamaterial was synthesized by nanosphere lithography and by depositing the plasmonic material, gold, by magnetron sputtering after a reactive ion etching process. As gain medium, it is used the laser dye styryl 9M embedded in a PMMA matrix.

The spatial and spectral coupling between the nanostructured material and the gain medium made possible a laser emission at a wavelength of 795 nm with a bandwidth (FWHM) of about 25 nm. The threshold for this laser phenomenon was found at about 1.2 mJ/cm^2 at a slightly higher value, but in agreement with the nanolaser devices in liquid recently demonstrated by T.Odom's group [11–13].

In the synthesized device, the laser emission was found at a angle 24° with an angular divergence of about 6°.

The nanosphere lithography technique used in the present work is a low cost technique with high volume productivity and it is not yet used in the literature to develop this type of devices. In fact, most of these devices are made by electron beam lithography or with the molding replica process.

In addition, a solid-state gain medium was used which allows greater integrability for a possible use as a coherent light source in integrated photonic systems or for lab-on-a-chip applications and high-performance chemical or biological sensors.

The numerous applications of this device and the potential developments make the laser light emission process from nanostructured materials a very interesting topic. The fundamental processes at the base of this device are also of current discussion: the role of the nanostructure order, the contribution made by the localized plasmon resonance, the role of scattering and absorption in the lasing process, the different mechanism of interaction between the active medium and the nanostructures as function of their mutual distance, the role of the quenching phenomenon of a fluorescent medium near a metal are still under debate and need to be investigated.

In addition to these questions, the possibility of studying different materials to be used both for the nanostructures and for the gain medium, makes the device adaptable to many situations. It would be possible in principle to explore the whole visible range, or think to a laser emission tunable by varying for example the grating period of the nanostructures or make multi-color devices implementing most gain media.

This opens the way to many studies in the future, both from the point of view of the understanding of the fundamentals physical processes controlling the lasing emission and for possible new applications of this device.

Appendix A

Styryl9M

In this appendix we show the characteristics of laser dye Styryl 9M. These characteristics are directly gotten from the producer, Lambda Physik, shown in the book *Laser Dye.*

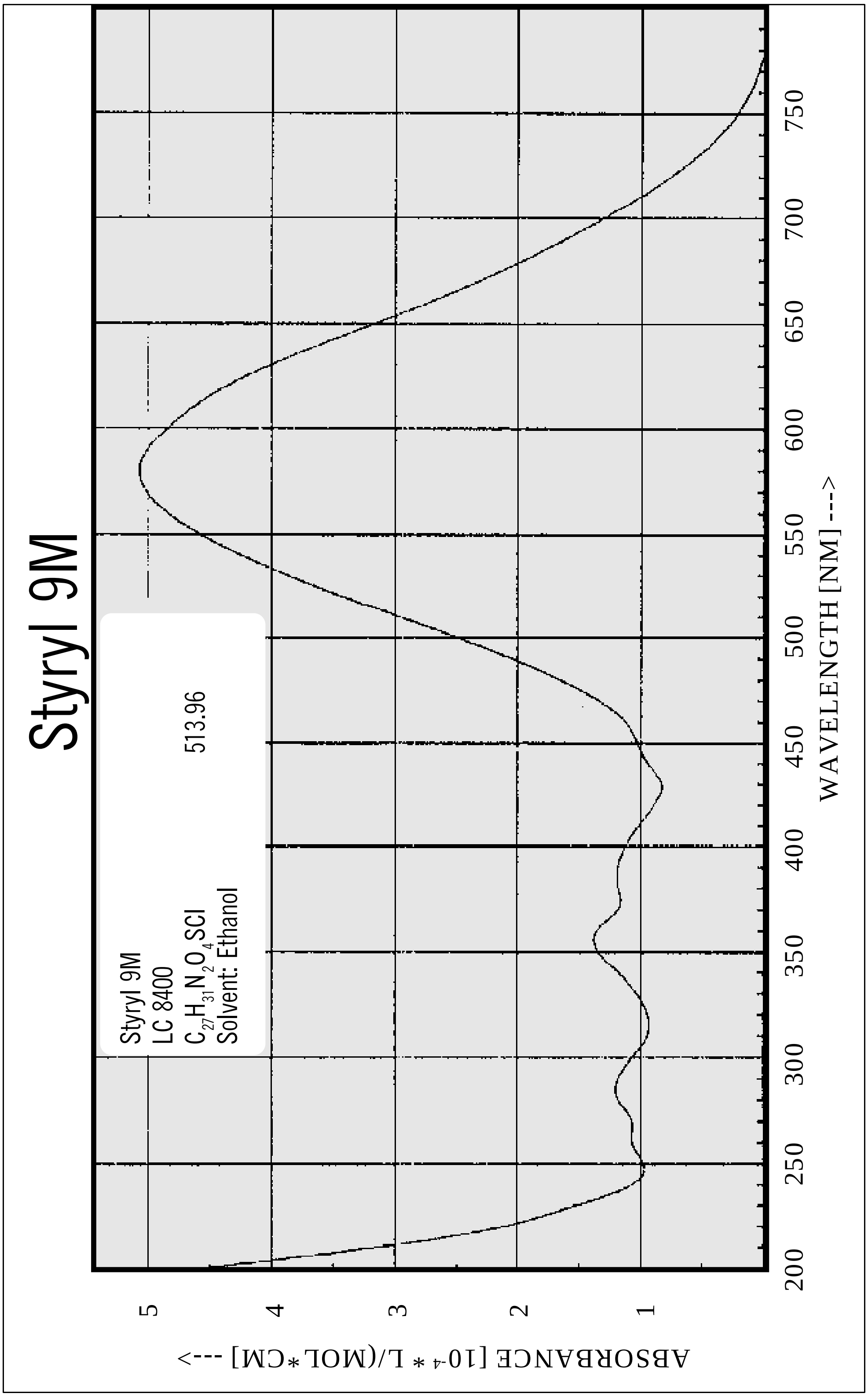
Styryl 9M
Styryl 9M
LC 8400
C27H31N2O4SCl
Solvent: Ethanol
513.96
ABSORBANCE [10-4 * L/(MOL*CM)] --->
5
4
3
2
1
WAVELENGTH [NM] --->
200
250
300
350
400
450
500
550
600
650
700
750

Styryl 9M (LC 8400)

Constitution

2-(6-(4-Dimethylaminophenyl)-2,4-neopentylene-1,3,5-hexatrienyl)-3-methylbenzothiazolium Perchlorat
LDS 821

$C_{27}H_{31}N_2O_4SCl$ · MW: 513.96

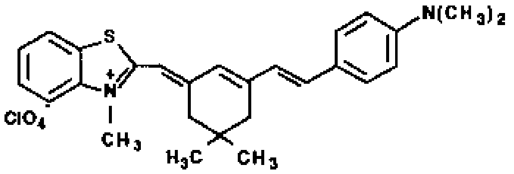

Characteristics

Lambdachrome® number:	8400
CAS registry number:	120528-73-6
Appearance:	green, crystalline solid
Absorption maximum (in ethanol):	585 nm
Molar absorptivity:	5.05×10^4 L mol^{-1} cm^{-1}
Fluorescence maximum:	-

For research and development purposes only.

Lasing Performance

Very efficient laser dye for pulsed and CW operation; tunable around 840 nm

Pump		*Dye Laser Characteristics*					
Source	*Wavelength [nm]*	*Peak [nm]*	*Range [nm]*	*Effic. [%]*	*Conc. [g/l]*	*Solvent*	*Ref.*
XeCl-Excimer	*308*	*840*	*810 - 875*	*9*	*1.10*	*DMSO*	*1,2*
Nitrogen	*337*	*840*	*803 - 875*	*rel.*	*1.03*	*DMSO*	*3*
Nd:YAG, 2nd	*532*	*824*	*797 - 851*	*15*	*0.26*	*Pc.*	*1, 4*
Cu-vapor	*510*	*815*	*793 - 845*	*14*	*0.67*	*Methanol*	*5*
Flashlamp	*-*	*840*	*810 - 860*	*-*	*0.01*	*Pc./Eg.*	*6, 7*
CW, Ar$^+$	*VIS*	*830*	*785 - 900*	*-*	*2.0*	*Pc./Eg.*	*1, 8,9*

References

See page 236.

P.S.

The 3-Ethyl-derivative (Styryl 9/LDS 820) shows similar performance. However, its photochemical stability in CW pumped dye lasers is slightly lower.

References (STYRYL 9M)

1. Lambda Physik, *Wall Chart* 1996.
2. V. S. Antonov, K. L. Hohla, *Appl. Phys.* B32, 9 (1983).
3. Lambda Physik, *Data Sheet.*
4. K. Kato, *IEEE J. Quantum Electr.* QE-16(19), 1017 (1980).
5. M. Broyer et al., *Appl. Phys.* B35, 31 (1984).
6. K. Smith, W. Sibbett, J. R. Taylor, *Opt. Commun.* 49(5), 359 (1984).
7. Cheng-Huei Lin, B. Marshall, *Appl. Optics* 23(14), 2228 (1984).
8. J. Hofnagle et al., *Opt. Commun.* 42(4), 267 (1982).
9. J. J. L. Mulders, L. W. G. Steenhuysen, *Opt. Commun.* 54(5), 295 (1985).

References (HITCI)

1. Lambda Physik, *Wall Chart* 1996.
2. H. Telle, W. Hüffer, D. Basting, *Opt. Commun.* 38(5,6), 403 (1981).
3. F. Bos, *Appl. Optics* 20(10), 3553 (1981).
4. Lambda Physik, *Data Sheet.*
5. F. Bos, *Appl. Optics* 20(20), 1886 (1981).
6. A. Hirth, K. Vollrath, J. Faure, D. Lougnot, *Opt. Commun.* 7(4), 339(1973).
7. Coherent, *CW Dye Laser Fact Sheets.*
8. T. F. Johnston, R. H. Brady, W. Proffitt, *Appl. Optics* 21(13), 2307 (1982).

References (IR 140)

1. Lambda Physik, *Wall Chart* 6/83.
2. F. Bos, *Appl. Optics* 20(20), 3553 (1981).
3. V. S. Antonov, K. L. Hohla, *Appl. Phys.* B30, 109 (1983).
4. Lambda Physik, *Data Sheet.*
5. F. Bos, *Appl. Optics* 20(10), 1886 (1981).
6. C. A. Moore, C. D. Decker, *J. Appl. Phys.* 49(1), 47 (1978).
7. C. D. Decker, *Appl. Phys. Letters* 27(11), 607 (1975).
8. J. P. Webb et al., *IEEE J. Quantum Electr.* QE-11, 114 (1975).
9. Coherent, *CW Dye Laser Fact Sheets.*
10. Lambda Physik.

List of Figures

Bibliography

[1] Ian Freestone, Nigel Meeks, Margaret Sax, and Catherine Higgitt. The lycurgus cup—a roman nanotechnology. *Gold Bulletin*, 40(4):270–277, 2007. 1

[2] Paolo Mazzoldi and G Mattei. Potentialities of ion implantation for the synthesis and modification of metal nanoclusters. *Rivista del Nuovo Cimento*, 28(7), 2005. 1

[3] Richard Feyman. There's plenty of room at the bottom: an invitation to enter a new field of physics. In *Annual conference of American Physical Society, California Institute of Technology, Pasadena*, volume 29, pages 5–22, 1959. 1

[4] Norio Taniguchi et al. On the basic concept of nanotechnology. In *Proc. Intl. Conf. Prod. Eng. Tokyo, Part II, Japan Society of Precision Engineering*, pages 18–23, 1974. 1

[5] S. A. Maier. *Plasmonics: fundamental and application.* Springer, 2007. 1, 5, 13

[6] R Gordon Gould. The laser, light amplification by stimulated emission of radiation. In *The Ann Arbor Conference on Optical Pumping, the University of Michigan*, volume 15, page 128, 1959. 2, 21

[7] Ifor David Williams Samuel and Graham Alexander Turnbull. Organic semiconductor lasers. *Chemical Reviews*, 107(4):1272–1295, 2007. 2

[8] Montacer Dridi and George C Schatz. Model for describing plasmon-enhanced lasers that combines rate equations with finite-difference time-domain. *JOSA B*, 30(11):2791–2797, 2013. 2, 28, 29

[9] Montacer Dridi and George C Schatz. Lasing action in periodic arrays of nanoparticles. *JOSA B*, 32(5):818–823, 2015.

[10] JP Martikainen, TK Hakala, HT Rekola, and P Törmä. Modelling lasing in plasmonic nanoparticle arrays. *Journal of Optics*, 18(2):024006, 2016. 2, 29

[11] Jae Yong Suh, Chul Hoon Kim, Wei Zhou, Mark D Huntington, Dick T Co, Michael R Wasielewski, and Teri W Odom. Plasmonic bowtie nanolaser arrays. *Nano Letters*, 12(11):5769–5774, 2012. 2, 27, 65

[12] Wei Zhou, Montacer Dridi, Jae Yong Suh, Chul Hoon Kim, Dick T Co, Michael R Wasielewski, George C Schatz, Teri W Odom, et al. Lasing action in strongly coupled plasmonic nanocavity arrays. *Nature Nanotechnology*, 8(7):506–511, 2013.

[13] Ankun Yang, Thang B Hoang, Montacer Dridi, Claire Deeb, Maiken H Mikkelsen, George C Schatz, and Teri W Odom. Real-time tunable lasing from plasmonic nanocavity arrays. *Nature Communications*, 6, 2015. 27, 65

[14] Hsin-Yu Wu, Longju Liu, Meng Lu, and Brian T Cunningham. Lasing emission from plasmonic nanodome arrays. *Advanced Optical Materials*, 2016. 2, 27

[15] A Hinke Schokker and A Femius Koenderink. Lasing in quasi-periodic and aperiodic plasmon lattices. *Optica*, 3(7):686–693, 2016. 2, 27

[16] M Vollmer and U Kreibig. *Optical properties of metal clusters.* Springer Ser. Mat. Sci, 1995. 5

[17] Charles Kittel. *Introduction to solid state.* John Wiley & Sons, 1966. 5

[18] Neil W Ashcroft and N David Mermin. *Solid State Physics.* Saunders College, 1976. 5

[19] Lukas Novotny and Bert Hecht. *Principles of nano-optics.* Cambridge University Press, 2012. 5, 17, 29

[20] Robert W. Boyd. *Nonlinear Optics.* Academic Press, 2003. 6

[21] Peter B Johnson and R-W_ Christy. Optical constants of the noble metals. *Physical Review B*, 6(12):4370, 1972. 8, 10, 11, 15

[22] F Hao and P Nordlander. Efficient dielectric function for fdtd simulation of the optical properties of silver and gold nanoparticles. *Chemical Physics Letters*, 446 (1):115–118, 2007. 8

[23] JJ Mock, M Barbic, DR Smith, DA Schultz, and S Schultz. Shape effects in plasmon resonance of individual colloidal silver nanoparticles. *The Journal of Chemical Physics*, 116(15):6755–6759, 2002. 12

[24] Catherine J Murphy, Tapan K Sau, Anand M Gole, Christopher J Orendorff, Jinxin Gao, Linfeng Gou, Simona E Hunyadi, and Tan Li. Anisotropic metal nanoparticles: synthesis, assembly, and optical applications. *The Journal of Physical Chemistry B*, 109(29):13857–13870, 2005. 12

[25] Gustav Mie. Beiträge zur optik trüber medien, speziell kolloidaler metallösungen (contributions to the optics of diffusing media). *Annalen der Physik*, 330(3):377–445, 1908. 12, 36

[26] Craig F Bohren and Donald R Huffman. *Absorption and scattering of light by small particles.* John Wiley & Sons, 2008.

[27] Uwe Kreibig and Michael Vollmer. *Optical properties of metal clusters*, volume 25. Springer Science & Business Media, 2013. 12

[28] R Gans. Fortpflanzung des lichts durch ein inhomogenes medium (propagation of light through a inhomogeneous medium). *Annalen der Physik*, 352(14):709–736, 1915. 12

[29] John David Jackson. *Classical electrodynamics*. Wiley, 1999. 14

[30] Huanjun Chen, Xiaoshan Kou, Zhi Yang, Weihai Ni, and Jianfang Wang. Shape- and size-dependent refractive index sensitivity of gold nanoparticles. *Langmuir*, 24(10):5233–5237, 2008. 15

[31] M Meier and A Wokaun. Enhanced fields on large metal particles: dynamic depolarization. *Optics Letters*, 8(11):581–583, 1983. 15

[32] Alexander Moroz. Depolarization field of spheroidal particles. *JOSA B*, 26(3): 517–527, 2009. 15

[33] Th Kokkinakis and K Alexopoulos. Observation of radiative decay of surface plasmons in small silver particles. *Physical Review Letters*, 28(25):1632, 1972. 15

[34] JC Maxwell Garnett. Colours in metal glasses and in metallic films. *Proceedings of the Royal Society of London*, 1904. 16

[35] Yu-lin Xu and Bo ÅS Gustafson. A generalized multiparticle mie-solution: further experimental verification. *Journal of Quantitative Spectroscopy and Radiative Transfer*, 70(4):395–419, 2001. 16

[36] Gaston Floquet. Sur les équations différentielles linéaires á coefficients périodiques. *Annales scientifiques de l'École normale supérieure*, 12:47–88, 1883. 16

[37] Felix Bloch. Über die quantenmechanik der elektronen in kristallgittern. *Zeitschrift für physik*, 52(7–8):555–600, 1929. 16

[38] Shengli Zou, Nicolas Janel, and George C Schatz. Silver nanoparticle array structures that produce remarkably narrow plasmon lineshapes. *The Journal of chemical physics*, 120(23):10871–10875, 2004. 17

[39] Uri Laor and George C Schatz. The role of surface roughness in surface enhanced raman spectroscopy (sers): the importance of multiple plasmon resonances. *Chemical Physics Letters*, 82(3):566–570, 1981. 17, 18

[40] Alastair D Humphrey and William L Barnes. Plasmonic surface lattice resonances on arrays of different lattice symmetry. *Physical Review B*, 90(7):075404, 2014. 19

[41] O Svelto. *Principles of Lasers*. Heidelberg: Springer, 2010. 21

[42] Anthony E Siegman. *Lasers*, volume 37. 1986. 21, 28, 29

[43] William T Silfvast. *Laser fundamentals*. Cambridge University Press, 2004. 21

[44] Albert Einstein. Zur quantentheorie der strahlung (on the quantum theory of radiation). *Physikalische Zeitschrift*, 18, 1917. 21

[45] HD Försterling and H Kuhn. *Physikalische Chemie in Experimenten, Verlag Chemie*. Weinheim, 1971. 26

[46] Joseph T Verdeyen. *Laser Electronics. 3ed.* Prentice Hall, 1995. 26, 71

[47] IP Kaminow, LW Stulz, EA Chandross, and CA Pryde. Photobleaching of organic laser dyes in solid matrices. *Applied Optics*, 11(7):1563–1567, 1972. 27

[48] T Bernas, M ZarEBski, RR Cook, and JW Dobrucki. Minimizing photobleaching during confocal microscopy of fluorescent probes bound to chromatin: role of anoxia and photon flux. *Journal of Microscopy*, 215(3):281–296, 2004. 27

[49] Michelle S Mackey and Wade N Sisk. Photostability of pyrromethene 567 laser dye solutions via photoluminescence measurements. *Dyes and Pigments*, 51(2): 79–85, 2001. 27

[50] Frerik van Beijnum, Peter J van Veldhoven, Erik Jan Geluk, Michiel JA de Dood, W Gert, and Martin P van Exter. Surface plasmon lasing observed in metal hole arrays. *Physical Review Letters*, 110(20):206802, 2013. 27

[51] Allen Taflove and Susan C Hagness. *Computational electrodynamics*. Artech House Publishers, 2000. 28

[52] Jan Trieschmann, Shumin Xiao, Ludmila J Prokopeva, Vladimir P Drachev, and Alexander V Kildishev. Experimental retrieval of the kinetic parameters of a dye in a solid film. *Optics Express*, 19(19):18253–18259, 2011. 29

[53] Klaus Böhringer and Ortwin Hess. A full-time-domain approach to spatio-temporal dynamics of semiconductor lasers. i. theoretical formulation. *Progress in Quantum Electronics*, 32(5):159–246, 2008.

[54] Sebastian Wuestner, Andreas Pusch, Kosmas L Tsakmakidis, Joachim M Hamm, and Ortwin Hess. Overcoming losses with gain in a negative refractive index metamaterial. *Physical Review Letters*, 105(12):127401, 2010. 29

[55] Pascal Anger, Palash Bharadwaj, and Lukas Novotny. Enhancement and quenching of single-molecule fluorescence. *Physical Review Letters*, 96(11):113002, 2006. 29, 30

[56] JA Rogers and RG Nuzzo. Nanostructured plasmonic sensors. *Chem Rev*, 108(2): 494521, 2008. 31

[57] Huaqing Li and Nianqiang Wu. A large-area nanoscale gold hemisphere pattern as a nanoelectrode array. *Nanotechnology*, 19(27):275301, 2008. 31

[58] Henry I Smith. 100 years of x rays: Impact on micro-and nanofabrication. *Journal of Vacuum Science & Technology B*, 13(6):2323–2328, 1995.

[59] TA Savas, ML Schattenburg, JM Carter, and Henry I Smith. Large-area achromatic interferometric lithography for 100 nm period gratings and grids. *Journal of Vacuum Science & Technology B*, 14(6):4167–4170, 1996. 31

[60] Christy L Haynes and Richard P Van Duyne. Nanosphere lithography: a versatile nanofabrication tool for studies of size-dependent nanoparticle optics. *The Journal of Physical Chemistry B*, 105(24):5599–5611, 2001. 31

[61] J Rybczynski, U Ebels, and M Giersig. Large-scale, 2d arrays of magnetic nanoparticles. *Colloids and Surfaces A: Physicochemical and Engineering Aspects*, 219(1): 1–6, 2003. 32

[62] Nikolai D Denkov. Two-dimensional crystallization. *Nature*, 361(6407):26, 1993. 35

[63] Takashi Yamasaki and Tetsuo Tsutsui. Fabrication and optical properties of two-dimensional ordered arrays of silica microspheres. *Japanese journal of applied physics*, 38(10R):5916, 1999. 37

[64] Stephen M Rossnagel, Jerome J Cuomo, and William Dickson Westwood. *Handbook of plasma processing technology: fundamentals, etching, deposition, and surface interactions*. William Andrew, 1990. 38

[65] Donald M Mattox. *Handbook of physical vapor deposition (PVD) processing*. William Andrew, 2010. 40

[66] Gerd Binnig, Calvin F Quate, and Ch Gerber. Atomic force microscope. *Physical Review Letters*, 56(9):930, 1986. 47

[67] David Nečas and Petr Klapetek. Gwyddion: an open-source software for spm data analysis. *Open Physics*, 10(1):181–188, 2012. 49

[68] Brent F Howell and Mark G Kuzyk. Amplified spontaneous emission and recoverable photodegradation in polymer doped with disperse orange 11. *JOSA B*, 19 (8):1790–1793, 2002. 57

[69] Otto Loebich. The optical properties of gold. *Gold Bulletin*, 5(1):2–10, 1972. 62